



Theory and experiment of nanostructure self-organization in irradiated materials

N.M. GHONIEM^a, D. WALGRAEF^{b,*} and S.J. ZINKLE^c

^a *Mechanical and Aerospace Engineering Department, The University of California at Los Angeles, Los Angeles, California 90095, U.S.A.*

^b *Center of Nonlinear Phenomena and Complex Systems, Free University of Brussels, CP 231, Bd du Triomphe, B-1050 Brussels, Belgium*

^c *Metals and Ceramics Division, Oak Ridge National Laboratory, P.O. Box 2008 MS6138, Oak Ridge TN 37831-6138, U.S.A.*

Received 14 April 2001; Revised 15 June 2001; Accepted 29 June 2001

Abstract. Irradiation of materials by energetic particles (e.g., electrons, ions and neutrons) is associated with very high internal power dissipation, which can drive the underlying nano- and microstructure far from normal equilibrium conditions. One of the most unusual responses in this connection is the ability of the material's nano- and microstructure to self-assemble in well-organized, two- and three-dimensional periodic arrangements. We review and assess here experimental evidence and theoretical models pertaining to the physical understanding of nano- and microstructure self-organization under irradiation conditions. Experimental observations on the formation of self-organized defect clusters, dislocation loops, voids and bubbles are presented and critically assessed. Implantation of metals with energetic helium results in remarkable self-assembled bubble super-lattices with wavelengths (super-lattice parameters) in the range of 5–8 nm. Ion and neutron irradiation produce a wide variety of self-assembled 3-D defect walls and void lattices, with wavelengths that can be tailored in the range of 10's to 100's of nanometers. Theoretical models aimed at explaining these observations are introduced, and a consistent description of many features is outlined. The primary focus of the most recent modeling efforts, which are based on stability theory and concepts of non-linear dynamics, is to determine criteria for the evolution and spatial symmetry of self-organized microstructures. The correspondence between this theoretical framework and experimental observations is also examined, highlighting areas of agreement and pointing out unresolved questions.

1. Introduction

The phenomena of pattern formation and self-organization have been viewed as natural responses of complex systems to strong external stimulation. The collective interaction between system components under external driving forces that drive the system far from equilibrium results in the self-organization of its constituents (e.g., [1–4]). Some of the salient successes of this viewpoint can be found in the behavior of chemical (e.g., [5, 6]), liquid crystal nematics (e.g., [7, 8]), and fluid systems (e.g., [9, 10]). It has also been recognized that condensed matter systems show a rich variety of patterns and self-assembled microstructures under conditions as diverse as solidification [11], electro-chemical deposition [12], plastic deformation (e.g., [13, 14]), surface modifications [15], rapid laser heating [16], irradiation by energetic particles [17], magnetic domains [18], and more recently, atom deposition into self-assembled monolayers [19–22]. The particular situation of energetic particle irradiation is quite interesting, and we plan to focus our attention in this article on reviewing the current understanding of the

*Director of Research at the Belgian National Fund for Scientific Research.

underlying physical mechanisms. The existence of an extensive experimental database in this area, and the concurrent evolution of contemporary theoretical frameworks allow us to present a broad perspective on the physical nature of self-organization in irradiated materials.

During the last three decades, numerous experimental observations on irradiated materials have systematically demonstrated the existence of fully or partially ordered nano- and microstructure in materials under energetic particle irradiation. The phenomenon appears to be of a general nature, and not confined to one type of microstructure. Voids, precipitates, vacancy clusters, Stacking Fault Tetrahedra (SFT's), gas bubbles and Self-Interstitial-Atom (SIA) clusters have all been observed to be spatially arranged in nano-scale, self-assembled patterns of typical dimensions 2–3 orders of magnitude greater than the atomic spacing. Striking observations have shown that in some cases, complete spatial isomorphism exists between the periodic structure of defect distributions and that of the fundamental atomic lattice. These experimental observations are particularly true for the spatial ordering of bubble and void microstructures in irradiated materials [23-30]. Singh and Evans [31] have recently reviewed the experimental results obtained on defect production and accumulation in irradiated materials, and emphasized the systematic differences between void and defect clusters in FCC and BCC metals and alloys. An important characteristic of void and bubble lattices is their spatial orientation along crystallographic directions, at least for the three main metal structures (FCC, BCC, and HCP). Jäger and Trinkaus reviewed the experimental observations of ordered defect structures in irradiated materials, and concluded that the isomorphy of the ordered defect structures with the host lattice is due to elastic interactions in the case of defect walls and anisotropic defect transport in the case of bubble and void superlattices [32].

The implications of understanding the physical nature of nano- and microstructure self-organization are quite clear from a technological perspective. The relationships between the material's microstructure and its mechanical and physical characteristics are established by a combination of experimental, empirical and theoretical methods. It is expected, therefore, that a physical understanding of the nano- and microstructure and its dependence on irradiation and material conditions would lead to better approaches to the design of radiation-resistant materials in nuclear technologies (e.g., fission and fusion energy). At the same time, ion, plasma and electron beam processing are becoming valuable tools in the manufacturing of electronic, photonic and microelectromechanical (MEMS) devices. While the impact of a physical understanding of nano- and microstructure self-organization phenomena on the variety of technologies discussed here is difficult to assess, the intrinsic scientific value is quite valuable. The collective behavior of constituents in hydrodynamic, chemical and liquid crystal systems has been systematically shown to result in pattern formation driven by dynamical instabilities. In the solid state, however, few examples exist, where the link between dynamical instabilities and the evolution of a self-organized nano- and microstructure has been clearly established. For example, while self-organized dislocation microstructure has been widely observed under cyclic and monotonic deformation conditions (e.g., Persistent Slip Bands, dislocation arrays, cells and subgrains), the reasons for its emergence have not yet been established [33]. Considerable recent interest in self-assembled nanophase materials has been driven by possible utilization in micro-electronics [20–22], photonics, biomedical and other nano-technology applications [19].

Concepts on the behavior of dynamical systems have been successfully applied to the problem of microstructure evolution in irradiated materials. Self-organization of irradiated microstructures can thus be viewed as one of the few examples in the solid state, where patterning can be directly linked to the collective dynamical behavior of constituent defects.

The aim of this work is to review current models of self-organized microstructure in irradiated materials, and compare the theoretical findings with experimental observations. Our plan is to first give a brief review of theoretical models in Section 2. In Section 3, we present an overview of the main experimental findings on microstructure self-organization. In Section 4, dynamical models that have contributed to our understanding of the phenomenon of irradiation-induced self-organization in metals are outlined. In Section 5, a general reaction-diffusion model, based on the evolution of mobile and immobile defects is analyzed within the framework of nonlinear dynamics, instability and pattern formation theory. Relevance of the theoretical approaches described in Sections 4 and 5 to experimental observations is discussed in Section 6. Finally, conclusions are drawn in Section 7.

2. Modeling approaches

Since the first reported observations of void lattices in irradiated materials, many theoretical attempts and models have been made to explain their formation and properties. These models may be divided into five main classes, according to the mechanism on which they are based [34]:

1. Elastic interactions.
2. Isomorphic decomposition.
3. Anisotropic SIA diffusion.
4. Cavity-interstitial loop interaction.
5. Nonequilibrium phase transitions, leading to self-organization.

The first two approaches are based on static elastic energy minimization arguments, and they have been mainly developed to explain void lattice formation. In the first case [35], the anisotropy of the elastic constants is responsible for the interaction between voids in irradiated materials. While void-void elastic interaction is strong when voids are closely separated, the short-range of the elastic interaction forces does not explain how voids and bubbles organize themselves over relatively long distances, especially during the early stages of irradiation. The second approach is based on the analogy [36] between void lattice formation and the ordering that occurs during precipitation and aging of alloys [37]. In these theories, however, the energy minima rarely correspond to the observed void lattice parameters or symmetries [34].

In the third approach, an important family of models, originating in the early approach of Foreman [38], are based on the effect of the anisotropic diffusion of SIAs' on the alignment of voids with the underlying crystal lattice. One- and two-dimensional models of this type have been developed, where transport of SIAs' is preferentially invoked along close-packed directions (1-D), or on highly-packed atomic planes. In the one-dimensional versions, it is argued that the motion of SIA along a particular direction could be responsible for void alignment along that direction, since unaligned voids would always receive a larger flux of SIAs' than aligned ones. As a result, unaligned voids should always move towards linear alignment. Since the preferred directions for SIA diffusion are the close-packed directions of the crystal, the final stable void lattice should have close-packed directions parallel to the host crystal lattice. Such ideas have been adapted by Woo and Frank in building of a two-interstitial model, where a key element is a postulated crowdion configuration of SIA [39, 40]. In a series of papers [26, 34, 41, 42], Evans developed a two-dimensional SIA diffusion model, induced by the fact that cavities may spatially order on planes parallel to the planes of SIA diffusion. This mechanism of void ordering is not a direct extension of the one-dimensional mechanism, but is based on a

detailed evaluation of SIA fluxes received by voids as a function of their spatial arrangement. The outcome is that the growth of aligned voids, resulting from the balance between vacancy and interstitial fluxes, is faster than for isolated ones, which shrink.

In the fourth approach, other models have been proposed, which consider the interaction between interstitial loops and cavities as the main selection mechanism of the void microstructure [43]. In this class of models, void lattice structure selection is of Darwinian type [40]: there is a selective growth and shrinkage process, and only the ‘fittest’ void structure survives. Hence, these models favor equilibrium-type concepts rather than dynamical ones. They also require preexisting random distributions of voids and point defects. They essentially depend on defect mobility, but not on defect production rates nor interactions. Their sensitivity to experimental parameters, such as irradiation dose, temperature, dislocation densities, etc., is difficult to assess. Furthermore, it is now realized that spatially uniform point defect and dislocation distributions may easily become unstable under irradiation. Hence, the resulting defect microstructure should also affect cavity distributions.

In the fifth and last modeling approach, the basic physical mechanisms, which control the interaction between defect populations have been identified. When highly energetic particles (electrons, neutrons, ions, α particles, etc.) interact with lattice atoms and transfer an energy larger than the displacement threshold, Frenkel pairs (vacancies and interstitials) are generated. A fraction of those Frenkel pairs are clustered as small interstitial aggregates, vacancy loops or SFTs. Furthermore, computer simulation studies of collision cascades using molecular dynamics have shown that interstitial clusters can be directly produced in the neighborhood of cascades [44-48], and can rapidly move along preferred close-packed directions. Implications of this direct production process to swelling and other macroscopic phenomena have been discussed by Zinkle and Singh [49], and by Woo et al. [50]. However, beyond some threshold determined by material and irradiation parameters to be discussed later, uniform distributions of vacancy and interstitial clusters become unstable. This instability induces spatial organization of defect populations, including vacancy and interstitial loops, and eventually trigger the formation of void and bubble lattices.

The following general conditions appear to be determine the formation of an ordered defect microstructure:

1. Agglomeration of vacancies into clusters (i.e., vacancy loops), perhaps directly during the collisional phase of cascade cooling.
2. A bias for dislocations towards preferential absorption of interstitials over vacancies (i.e., absorption asymmetry).
3. An asymmetry in the production and diffusion of mobile point defects (i.e., production bias).
4. Some degree of anisotropy during the evolution of clustered defects. This could either be triggered by diffusional anisotropies of point defects, or by anisotropic elastic interaction between defect clusters during the latter stages of their evolution.

Although these mechanisms do not necessarily affect defect cluster shapes, they determine the symmetries of their spatial distributions and thus the symmetry of the nano- and microstructure itself. The first two conditions seem to be necessary for the onset of a spatial instability in the nano- and microstructure, while the existence of the last two conditions contributes to either the onset of nano- and microstructure instability, or the spatial symmetry of its evolution. Krishan was the first to search for a coherent understanding of these phenomena within the framework of irradiation-induced self-organization of material defects [51]. In this approach, rate equations describing the evolution of each relevant defect den-

sity are derived. Uniform solutions are searched, and their stability versus inhomogeneous perturbations analyzed. Instability criteria which depend on kinetic rate coefficients, and thus on material parameters, may then be found. Various authors have proposed different types of models describing the evolution of relevant defect densities under irradiation [52–63]. Basic models take into account dynamical equations for two mobile atomic species (vacancies and interstitial atoms), and at least one basic immobile element of the microstructure (e.g., vacancy clusters). More detailed descriptions include interstitial clusters, voids or bubbles. These equations are based on the fundamental elements of defect dynamics, namely, point defect creation, recombination and migration to the microstructure. The combination of non-linear interactions, bias and mobility differences between several defect populations easily induces pattern forming instabilities. However, and similar to other pattern forming systems, a complete analysis of microstructure formation requires not only the derivation of instability criteria through linear stability analysis of uniform defect distributions, but also nonlinear analysis of the post-bifurcation regime. In particular, the symmetry, orientation and stability of the selected nano- and microstructure depend crucially on nonlinear interactions between unstable spatial modes [64].

3. Experimental observations of self-assembled nanostructures

Experimental observations of self-organized nano- and microstructure have shown that irradiation with energetic particles can result in void lattice formation [17, 29, 30], bubble lattice formation [23–25], precipitate ordering [26], defect walls and vacancy loop ordering [27, 28, 65]. In particular, experiments indicated that small defect clusters produced in irradiated face-centered-cubic (FCC) metals such as Ni [66–74] and Cu [65, 72] have a tendency to become aligned along {001} planes under certain conditions. The defect cluster alignment in Ni becomes noticeable at damage levels of 0.1 displacements per atom (dpa), and remains stable up to damage levels in excess of 20 dpa. The effects of irradiation spectrum or material variables on defect cluster pattern formation needs further clarification.

3.1. DEFECT CLUSTER PATTERNS

Due to their similar mass and FCC crystal structure, Ni and Cu are attractive for studying fundamental aspects of irradiation, such as defect clustering processes associated with displacement cascades. Low energy ion irradiation studies [75–81] have demonstrated that a higher density of visible vacancy clusters is produced in Cu compared to Ni over a wide range of irradiation temperatures. On the other hand, the amount of ion beam mixing [82] and the total surviving defect fraction (clustered and isolated point defects) associated with ion and neutron irradiation [83–87] have been found to be lower in Cu compared to that in Ni following irradiation near 4 K. These seemingly contradictory results can be interpreted as evidence for the presence of thermal spikes in displacement cascades. According to the thermal spike model, the lower melting point and weaker electron-phonon coupling in Cu compared to Ni both act to increase the duration and affected volume of the liquid-like region associated with a displacement cascade [44, 78–82]. The relatively large volume and slow cooling rate for the thermal spike in Cu promotes point defect recombination and leads to more pronounced clustering of the surviving defects.

Figs. 1 and 2 show a compilation of the published studies of defect cluster patterning in copper and nickel, in the form of plots showing the temperature and dose rates where {001}

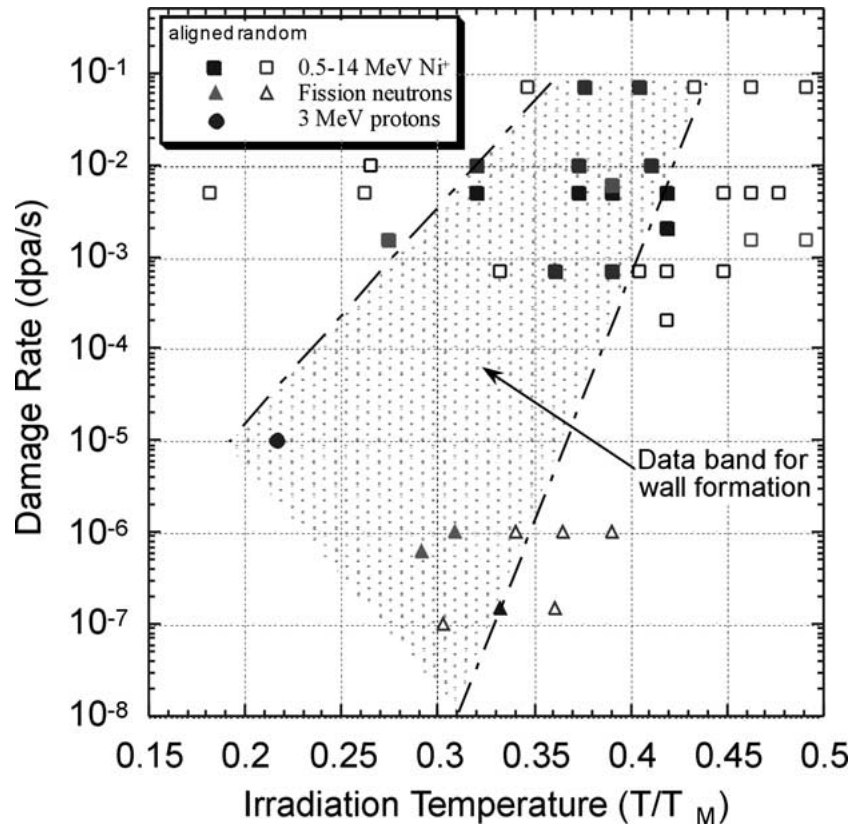


Figure 1. Data compilation showing the temperature and dose rates where {001} defect cluster wall formation has been observed in irradiated nickel. The data include Ni⁺ ion [66–68, 70], fission neutron [28, 74], and proton [65, 72] irradiations. The filled symbols denote conditions where defect cluster wall formation was observed.

defect cluster walls have been observed. As shown in Fig. 1, defect cluster patterning occurs in nickel at homologous irradiation temperatures between 0.2 and 0.42 T_m (depending on the dose rate) [66–74]. These studies have found that wall formation in Ni becomes observable at damage levels > 0.1 dpa, and is fully developed by 0.5 to 1 dpa [32, 74]. The cluster pattern apparently remains stable up to high damage levels; e.g., defect cluster patterning has been observed in Ni irradiated to 24 dpa with 500 keV Ni⁺ ions at 450 °C [69] and in Ni irradiated with 14 MeV Cu₃⁺ ions to dose > 50 dpa at 400 °C. One important feature is that the defect clusters contained in the {001} walls are predominantly vacancy in nature [32, 69]. According to theoretical arguments discussed in refs. [60, 63], self-organization of defect clusters into aligned patterns is expected only when the vacancy clusters are the dominant sink for interstitials and vacancies. Defect cluster alignment is generally not observed at high irradiation temperatures due to thermal dissolution of vacancy clusters (recovery Stage V) [32]. It has been proposed [32] that defect cluster ordering is suppressed at low temperatures and high damage rates because point defect matrix recombination becomes the dominant annihilation mechanism (as opposed to annihilation at defect clusters). Fig. 2 shows the corresponding dose rate-temperature plot for defect cluster patterning in irradiated copper [65, 72, 88–91]. The most striking feature in this plot is the lack of defect cluster wall formation in copper at irradiation conditions which caused significant {001} wall formation in nickel. Neglecting electron irradiation studies which will be discussed later, defect cluster wall formation has

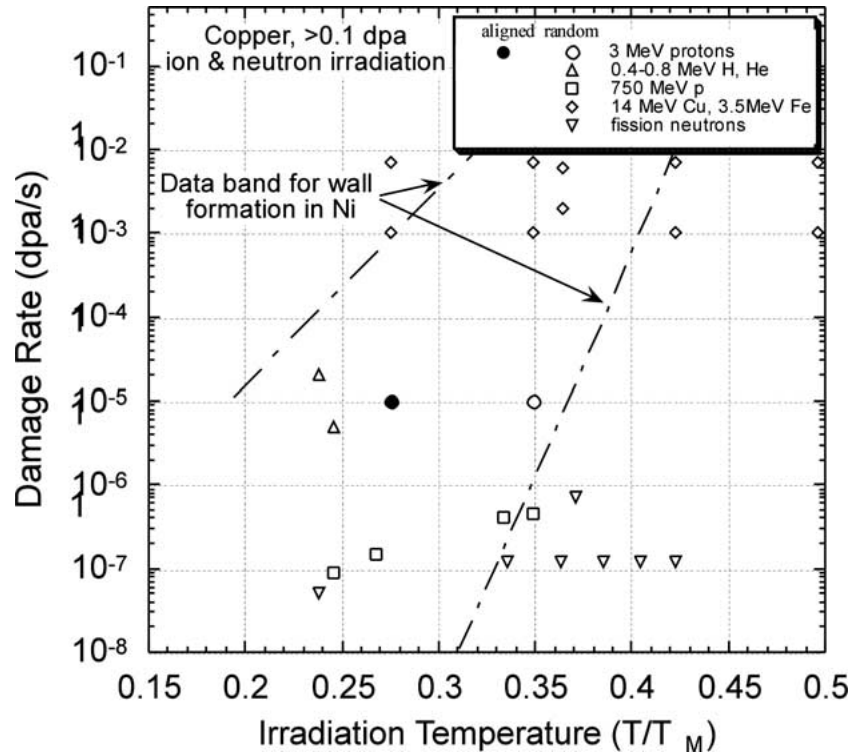


Figure 2. Microstructural observations of the absence (open symbols) or presence (filled symbols) of aligned defect cluster walls in irradiated copper. The dashed lines outline the data band for observations of wall formation in irradiated nickel (Fig. 1). The Cu data include 0.4 MeV protons [100], 0.8 MeV He ions [100], 3-MeV protons [72, 65], 750-MeV protons [91], Cu+ ions [88], Fe+ ions [134], and fission neutrons [74, 89–91].

only been observed in copper irradiated with 3-MeV protons at 100 °C [65, 72]. The 3-MeV proton irradiation were performed at a dose between 0.01 and 4 dpa, and defect cluster patterning was fully developed in Cu specimens irradiated to a dose > 0.7 dpa. The accumulated dose in some of the studies plotted in Fig. 2 (0.2 dpa) may have been too low to allow the full development of defect cluster patterning in Cu. However, some evidence of pattern formation should have been detectable, since defect cluster patterning was observable in neutron-irradiated Ni [74] and 3-MeV proton-irradiated Cu [72] at damage levels of 0.1 dpa. The dose levels attained in the other studies plotted in Fig. 2, where defect cluster patterning was not observed, ranged from 0.4 to 40 dpa. Defect cluster patterning has not been reported in numerous other irradiation studies on copper (e.g., [92–94]) that were performed under dose, dose rate and temperature conditions which should have been favorable for wall formation based on the behavior of nickel. However, these data have not been included in Fig. 2 because it is uncertain if the authors examined the microstructure under imaging conditions which would clearly reveal the presence or absence of defect cluster patterning.

Several different studies have observed the presence of aligned defect clusters in thin foils of copper [95–99] and nickel [99] following electron irradiation. Regular arrays of SFTs along $\langle 001 \rangle$ have been observed in copper during electron irradiation at temperatures between 170 and 350 K (0.12 to 0.26 T_m) and in nickel at temperatures between 380 and 540 K (0.22 to 0.31 T_m) [99]. In summary, it appears that defect cluster patterning occurs readily in nickel in irradiation spectra ranging from high PKA energies (Ni+ ion and neutron) to low PKA

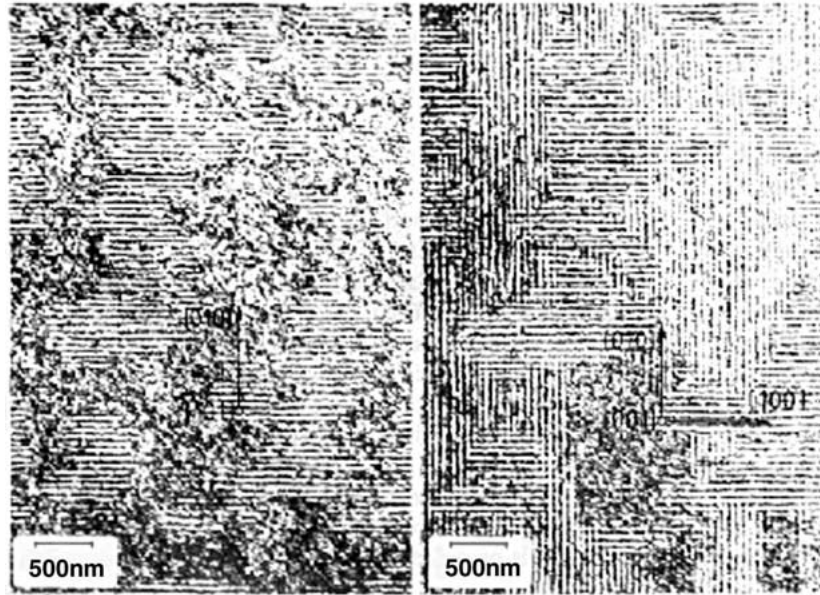


Figure 3. Dislocation microstructures (periodic arrays of vacancy loops) in Copper irradiated with protons, at an irradiation dose of 2 dpa (courtesy of W. Jäger [65, 72].)

energies (3 MeV protons and 1 MeV electrons). On the other hand, defect cluster pattern formation has so far only been observed in copper specimens exposed to 3 MeV protons. The dislocation loop microstructure revealed by TEM observations of Jäger and coworkers [65, 72] is shown in Fig. 3. Further TEM studies on copper irradiated at temperatures between 0 and 200 °C at damage rates between 10^{-6} and 10^{-4} dpa s^{-1} are needed to further investigate this apparent resistance to defect cluster patterning in irradiation spectra with high PKA energies.

The absence of defect cluster patterning in irradiated copper (except for the 3 MeV proton results) does not appear to be associated with a displacement cascade energy effect, since patterning was not observed in copper irradiated with 0.4 MeV H or 0.8 MeV He ions to a dose of 0.2–2 dpa [100]. Ion and neutron irradiation studies indicate that the rate of defect cluster accumulation during neutron irradiation at homologous temperatures between 0.2 and 0.3 T_m , is approximately the same in both copper and nickel at low dose [74, 91]. However, the observed defect cluster density in nickel at a given dose is an order of magnitude smaller than that in copper. Both materials approach a saturation level in defect cluster density at a dose > 0.1 dpa. The saturation defect cluster density is apparently a factor of 5 lower in nickel than that in copper ($2 \times 10^{23} m^{-3}$ versus $1 \times 10^{24} m^{-3}$). The fraction of defects resolvable as SFTs (vacancy clusters) in Cu and Ni ranges between 50 and 90%, depending on dose [74].

A further difference between the microstructure of neutron irradiated copper and nickel is apparent at damage levels greater than 0.1 dpa. The interstitial dislocation loop size and density in nickel irradiated at homologous temperatures between 0.2 and 0.3 T_m increase steadily with increasing dose, and the loop density exceeds the SFT density ($10^{23} m^{-3}$) at damage levels greater than about 0.1 dpa [74]. On the other hand, the resolvable (> 5 nm diameter) interstitial loop density in copper irradiated in this temperature range remains below $10^{21} m^{-3}$, at least up to damage levels of 1 dpa [91]. The displacement dose dependence of the defect cluster density at irradiation temperatures of 0.2–0.3 T_m is shown in Fig. 4. The cluster densities in irradiated Ni is generally an order of magnitude smaller than those found

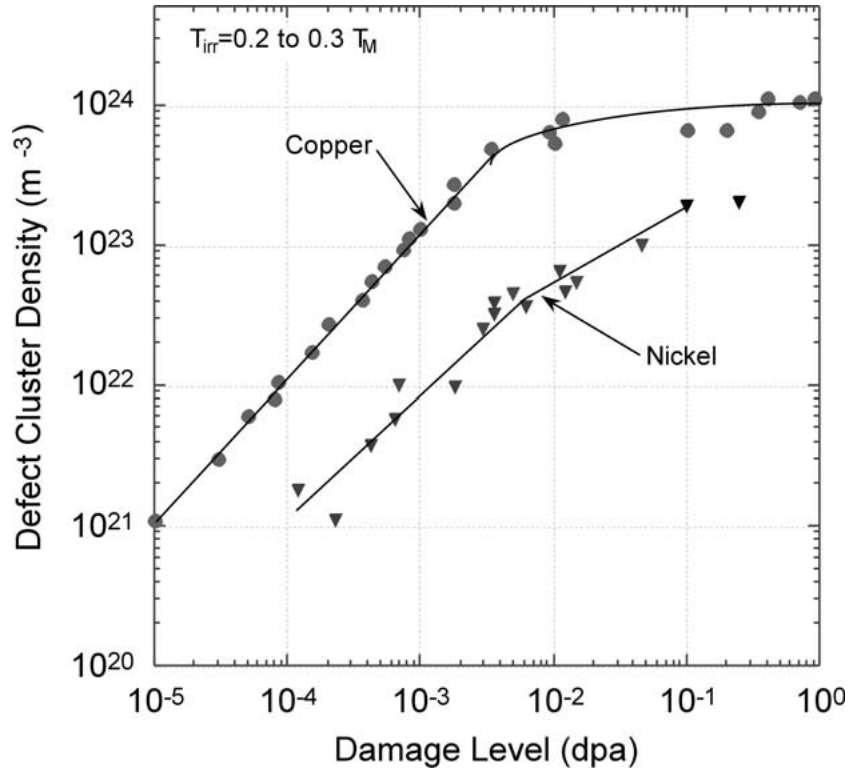


Figure 4. Comparison of the dose-dependent defect cluster density in nickel and copper irradiated with neutrons at low temperatures. Details about the original references are given elsewhere [74].

in Cu, except at doses above 0.1 dpa, where the density ratio drops to $\simeq 4-5$. According to conventional chemical rate theory predictions, the homogeneous interstitial loop nucleation and growth rates should be similar in Cu and Ni because the interstitial atomic volumes are similar. This suggests that there may be some difference in the initial disposition of interstitials (clustered vs. isolated fraction) produced in displacement cascades in copper compared to nickel. A similar conclusion was reached by Watanabe et al. [101] during their evaluation of in-cascade defect cluster formation in 14-MeV neutron irradiated copper and nickel.

Molecular dynamics (MD) simulations indicate that significant differences exist between the cascade quench behavior of Cu and Ni [44–48]. The MD studies suggest that the duration and affected volume of the ‘thermal spike’ is larger in copper compared to nickel, which results in increased clustering and a lower surviving defect fraction in Cu for a given PKA energy. According to the thermal spike model, the longer thermal spike lifetime in Cu is due to the lower melting point and less efficient electron-phonon coupling [44–46, 102–105]. Another parameter of interest is the size distribution of defect clusters produced in displacement cascades in copper versus nickel. The larger size and longer duration of the thermal spike in copper should result in a larger average cluster size for both vacancies and interstitials. In addition, the order of magnitude larger vacancy mobility in Cu compared to Ni near their melting points may enhance the formation of vacancy clusters in Cu during the thermal spike [106]. Recent MD studies suggest that small defect clusters containing up to 6 interstitials are highly glissile along $\langle 110 \rangle$ directions [47]. Therefore, it seems conceivable that the relative

proportion of interstitial clusters produced in displacement cascades between small (glissile) and large (sessile) clusters could have a strong influence on self-organization in metals.

The formation of aligned {001} defect cluster patterns in irradiated Cu and Ni may be attributable to the migration of glissile interstitial clusters along $\langle 110 \rangle$ directions [32]. A similar mechanism (based on dynamic crowdion migration) was proposed by Seeger and coworkers [99] to explain the presence of SFT ordered arrays in electron-irradiated FCC metals. However, it seems unlikely that dynamic crowdions could account for the wall formation observed for example in Ni at temperatures between 0.2 and 0.4 T_m since crowdions would not be thermally stable in this temperature regime. The low temperature limit of 0.12 T_m in Cu for defect cluster pattern formation during electron irradiation [99] is consistent with the onset of recovery Stage II [107]. Recovery Stage II has generally been attributed to rearrangement of interstitial clusters that either nucleated homogeneously or else directly in the displacement cascade [107]. Diffuse X-ray scattering measurements performed on irradiated FCC metals [107, 108] indicate that small interstitial clusters become mobile and coarsen during recovery Stage II. Therefore, it seems reasonable to associate the broad recovery Stage II with the migration of various sizes of glissile interstitial clusters (each having a different activation energy). The lower temperature limit for defect cluster patterning during electron irradiation (170 K in Cu) would then be associated with the minimum temperature for migration of small glissile interstitial clusters.

Table 1 gives a summary of experimental observations of defect pattern formation in irradiated FCC metals. Only defect walls or labyrinth structures have been observed in FCC metals irradiated with ions or neutrons [109]. With the exception of the low-temperature, low dose rate neutron irradiated aluminum [32], the experimentally-observed wavelength of defect walls and labyrinth structures is in the limited range of 30–90 nm. It should also be noted that defect cluster patterning is not observed in Cu and Ni, when they are pre-implanted with H or He [72]. Loop patterning has also been reported for ion and neutron irradiated Mo and Mo-0.5%Ti-0.1%Zr [110].

3.2. VOID AND BUBBLE PATTERNS

Within a few years following the discovery of radiation-induced void formation in metals, researchers determined that ordered arrays of voids could be formed under certain conditions [17, 30, 66]. Subsequently, it was also found that ordered arrays of gas-filled cavities (bubbles) could be produced in metals by ion implantation [23, 112]. Many of the experimental observations of void and bubble superlattice formation have been summarized in previous reviews [32, 34, 53, 66, 113]. An updated summary of the key features from the experimental studies performed to date is given in the following. This summary will not discuss the numerous observations of solid precipitates formed in metals implanted with inert gases [114]. In addition, results on the formation of periodic arrays of cavities in HCP metals will not be summarized here since they have been adequately reviewed elsewhere [32, 34, 53, 113]. It has been observed that the ordered void and bubble lattices in HCP metals are typically located in two-dimensional layers parallel to the basal plane. In contrast, the cavity lattice in FCC and BCC metals adopts the same three-dimensional symmetry as the host lattice. The experimental observations of void superlattice formation in irradiated BCC and FCC metals are summarized in Table 2 [17, 29, 30, 66, 110, 11, 115–117]. Voids initially form randomly in irradiated materials, and then gradually transform to an ordered array under some experimental conditions. The threshold dose for initial development of visible void ordering

Table 1. Summary of defect cluster patterning observations in irradiated FCC metals

Metal	Irradiation conditions	Cluster density $\times 10^{-22}$ (m^{-3})	Experimental λ (nm)
Ni [66]	5 MeV Ni+; 280-450°C; 5×10^{-3} dpa s^{-1} ; 15 dpa	4	40
Ni [67]	5 MeV Ni+; 280°C; 5×10^{-3} dpa s^{-1} ; 1-15 dpa	4	35
Ni [67]	5 MeV Ni+; 370°C; 5×10^{-3} dpa s^{-1} ; 1-15 dpa	3.3	40
Ni [67]	5 MeV Ni+; 423°C; 5×10^{-3} dpa s^{-1} ; 1-15 dpa	2	45
Ni [68]	2.8 MeV Ni+; 350-400°C; 7×10^{-4} dpa s^{-1} ; 13 dpa	1-3.5	30-42
	2.8 MeV Ni+; 375-425°C; 7×10^{-2} dpa s^{-1} ; 13 dpa	2.4-6.5	30-42
Ni [69]	0.5 MeV Ni+; 450°C; 2×10^{-3} dpa s^{-1} ; 24 dpa	5	40-45
Ni [70]	14 MeV Ni+; 200°C; $0.15 - 1.5 \times 10^{-3}$ dpa s^{-1} ; 0.7-7 dpa	2	40
	14 MeV Cu+; 400°C; $1.5 - 5 \times 10^{-3}$ dpa s^{-1} ; 30-100 dpa	2.2	41
Ni [71]	14 MeV Ni+; 400°C; $0.6 - 6 \times 10^{-3}$ dpa s^{-1} ; 5-50 dpa	5	35
Ni [72]	3 MeV H+; <100°C; 1×10^{-5} dpa s^{-1} ; 1.1 dpa	-	48
Ni [28]	Fission neutrons; 300°C; 5×10^{-7} dpa s^{-1} ; 1 dpa	>1	35
Ni [73]	Fission neutrons; 260°C; 1×10^{-6} dpa s^{-1} ; $\simeq 1$ dpa	-	-
Ni [74]	Fission neutrons; 230°C; 9×10^{-7} dpa s^{-1} ; 0.1 dpa	19	30-60
Ni [74]	Fission neutrons; 230°C; 9×10^{-7} dpa s^{-1} ; 0.25 dpa	20	45
Cu [72]	3 MeV H+; <100 °C; 1×10^{-5} dpa s^{-1} ; 0.1 dpa	-	25-90
Cu [72]	3 MeV H+; <100 °C; 1×10^{-5} dpa s^{-1} ; 0.65 dpa	-	60
Cu [72]	3 MeV H+; <100 °C; 1×10^{-5} dpa s^{-1} ; 2 dpa	$\simeq 0.1$	60
Al [28]	Fission neutrons; 55°C; 5×10^{-7} dpa s^{-1} ; 1 dpa	-	220

is a few dpa for BCC metals such as Mo, W and Nb [29 110, 111, 115, 116]. Fully developed (near-perfect ordering) void superlattices have been observed in irradiated BCC metals after dose levels of 30 dpa. Examples of TEM observations of near perfect Mo and Nb void lattices are shown in Figs. 5 and 6, respectively. In Fig. 5, a BCC void lattice is shown to develop in Mo irradiated with 2 MeV N+ ions to a dose of 100 dpa at 870 °C [135]. A Nb void lattice showing BCC isomorphism with the host lattice is shown in Fig. 6 for Nb irradiated with 7.5 MeV Ta+ ions to a dose of 300 dpa at 800 °C [66]. In contrast, the development of void superlattices in FCC metals apparently requires considerably higher damage levels of 100-400 dpa. There has been only one set of observations of a fully developed void superlattice in an FCC metal, namely pure nickel specimens which were ion irradiated to damage levels of 400 dpa [29, 66]. Imperfect (partially ordered) FCC void lattices have also been reported for irradiated Al [118-120], Ni-Al alloys [117], stainless steel [121] and Cu-10%Ni [122] specimens irradiated to damage levels of $\simeq 10$ -80 dpa.

The experimental observations suggest that void superlattice can be formed over a wide temperature range (comparable to the void swelling temperature range), although the void superlattice is most easily formed at temperatures just below the peak swelling temperature. The effect of alloying additions on void ordering is unclear. Several studies have observed similar void ordering behavior in Mo-0.5Ti [30, 110] and Nb-1Zr [116] alloys compared to the pure metals. Wiffen reported that void ordering was suppressed in Nb-1Zr compared

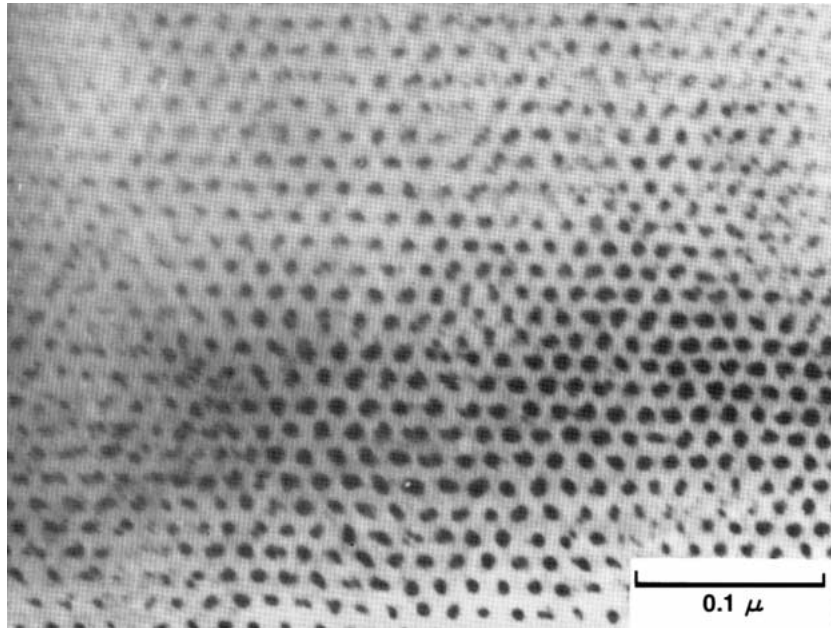


Figure 5. Mo void lattice: Electron micrograph showing a BCC void superlattice in molybdenum irradiated with 2 MeV N⁺ ions to a dose of 100 dpa at 870 °C [135]. The electron beam was parallel to the [111] crystal orientation. The micrograph was taken in an overfocused condition, which causes the voids to appear as dark spots.

to pure Nb [30]. However, it is possible that this difference may have been due to oxygen impurity effects rather than substitutional solute effects. Loomis observed that void ordering did not occur in Nb and Nb-1Zr specimens containing less than 60 ppm and 400 ppm oxygen, respectively [116].

The void lattice parameter is typically about two orders of magnitude larger than the atomic lattice parameter, and about four times larger than the void diameter in fully-developed void superlattices (cf., Table 2). The void lattice parameter has been reported to initially decrease with increasing dose as the superlattice is being formed [116], and then attains a constant value once the superlattice is fully developed [110, 111, 116]. The void lattice parameter decreases slightly with increasing damage rate (due to the effect of damage rate on the cavity density at a given temperature). The void lattice parameter increases with increasing irradiation temperature [110, 115, 116]. The ratio of the void lattice parameter to the void diameter tends to approach a value of 10 once the superlattice is fully developed [66, 116].

The void superlattice in BCC metals first becomes visible at volumetric swelling levels of 0.2–1%. Although the formation of a void superlattice can lead to reduced swelling rates, saturation in swelling does not necessarily occur when the void lattice is formed. For example, void swelling continued to steadily increase in ion-irradiated Mo specimens up to a dose of 150 dpa at 900 °C, whereas a void superlattice was clearly formed already at 10 dpa [111]. It is important to note that void superlattices have not been observed to date in vanadium or V alloys, despite high-dose irradiation studies performed up to 100 dpa which produced void densities of $0.1\text{--}2 \times 10^{22} \text{ m}^{-3}$ and swelling levels up to 3% and higher [30, 123, 124]. A robust theoretical model of the void ordering process should be capable of explaining the difficulty of void superlattice formation in vanadium (versus the relatively easy production

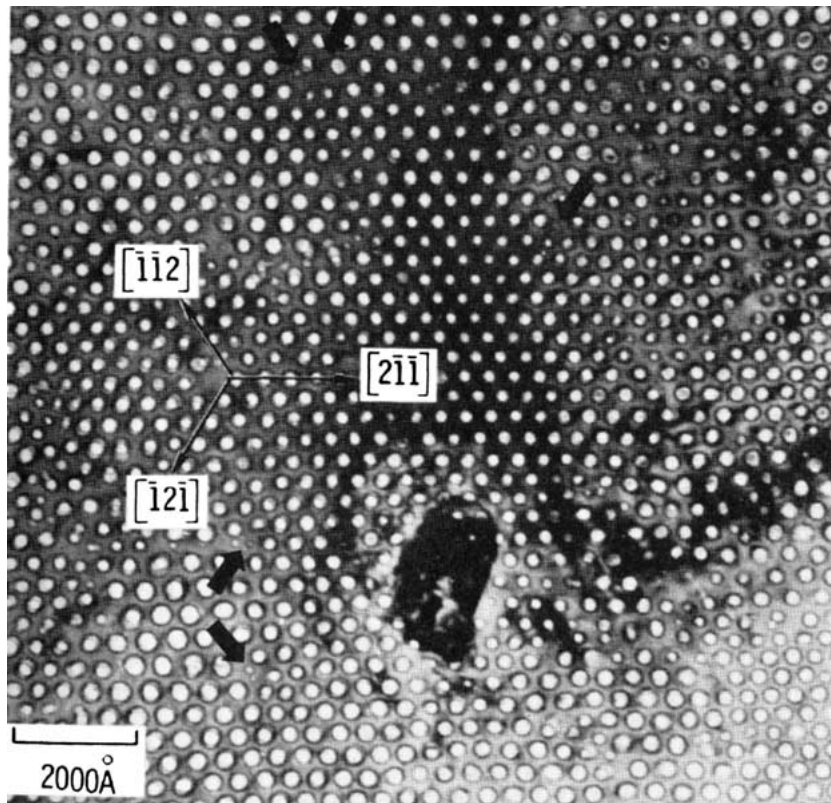


Figure 6. Nb void lattice: Electron micrograph showing a BCC void superlattice in niobium irradiated with 7.5 MeV Ta⁺ ions to a dose of 300 dpa at 800 °C [66]. The foil orientation is near [111].

of void superlattices in other BCC metals), and it should also describe why void ordering is much more difficult in FCC compared to BCC metals.

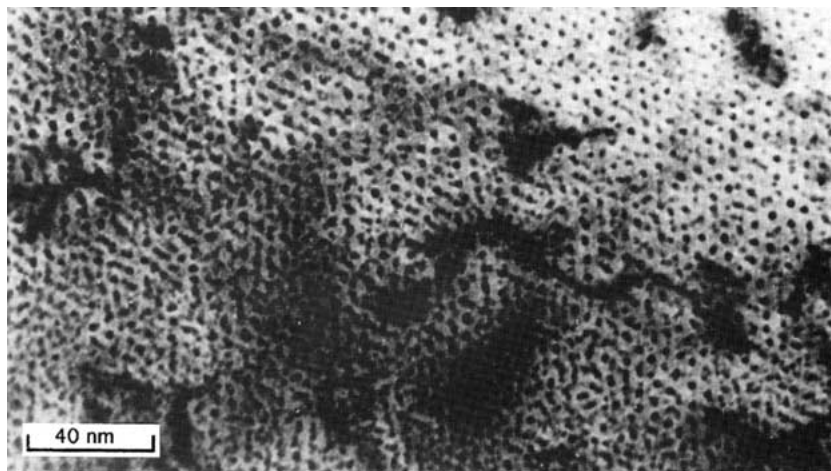


Figure 7. TEM observations of helium bubble lattice in Mo irradiated with 40 KeV helium at 500 °C to an ion flux of $5 \times 10^{21} \text{ m}^{-2}$ [113].

Table 3 summarizes the experimental observations of gas bubble superlattices in irradiated BCC and FCC metals [23, 66, 113, 125–127]. According to current understanding, bubble superlattices only occur in metals irradiated with gaseous ions at homologous temperatures between 0.15 and 0.35 T_m , where T_m is the melting temperature [23, 112]. A helium bubble superlattice was originally reported to form in Mo irradiated at room temperature ($\sim 0.1 T_m$) [23, 112]. Fig. 7 shows TEM observations of helium bubble lattice, formed by irradiating Mo with 40 KeV helium at 500 °C to an ion fluence of $5 \times 10^{21} \text{ m}^{-2}$ [113]. However, subsequent experiments determined that a helium bubble superlattice could only be formed at temperatures above 150 °C ($\sim 0.15 T_m$) [113]. It is likely that the actual irradiation temperature in the original studies on Mo may have been significantly higher than room temperature due to beam heating [113]. The critical fluence for formation of a helium bubble superlattice is $\simeq 4 \times 10^{21} \text{ m}^{-2}$ (just below the blistering fluence), which corresponds to an implanted He concentration of $\simeq 10\%$. The bubble lattice parameter appears to be independent of temperature over the limited temperature range where bubble superlattices are formed. The magnitude of the bubble lattice parameter does not appear to be dependent on physical properties of the host metal such as the shear modulus. The measured helium bubble lattice parameter ranges from 4 to 8 nm in different metals. The FCC noble metals (Cu, Au) have the largest bubble lattice parameter, whereas a BCC metal (vanadium) has the smallest bubble lattice parameter. The bubble lattice parameter is about three times the mean bubble diameter. A microscale helium bubble superlattice (70 nm bubble diameter, 105 nm bubble lattice parameter) has been observed to coexist with the usual (nanoscale) bubble superlattice in Au implanted at relatively high fluence [126].

4. The rate theory of nano-structure self-organization

In the rate theory approach, the evolution of defect populations, including voids, is described with dynamical models based on kinetic rate equations. These equations are analogous to chemical kinetic rate equations, and take into account defect production, motion and interactions. They are thus of the reaction-transport type. Radiation-produced defects are represented by two equations for mobile point defects (i.e. vacancies and interstitials), and a set of equations describing the evolution of loops, which are considered as immobile species. Since point defects are the only mobile components of the nano- and microstructure, their rate equations would include spatial operators. Immobile nano- and microstructures are represented by loops and voids as discussed below.

4.1. ORIGIN OF NANO-STRUCTURE INSTABILITIES

The formation of irradiation-induced defect nano- and microstructure as a consequence of spatial instabilities is discussed in [51, 54, 59]. It is based on the analysis of coupled rate equations describing the evolution of defect densities, and derived by Bullough, Eyre and Krishan [128]. The structure of these equations takes the form:

$$\begin{aligned} \dot{c}_r &= P_r - \alpha c_1 c_2 + \sum_r D_r \rho_q (\Phi_{qr} - Z_{qr} C_r) + D_r \nabla^2 c_r \quad (r = 1, 2), \\ \dot{Q}_q &= \epsilon_q P + (Z_{q1} D_1 c_1 - Z_{q2} D_2 c_2) \rho_q - \sum_r D_r \Phi_{qr} \rho_q \quad (q = 1, \dots, n). \end{aligned} \quad (1)$$

In this notation, c_r represent point defect densities ($r = 1$ corresponds to vacancies and $r = 2$ corresponds to interstitials), each of them being produced at an effective rate P_r , where P_r

Table 2. Summary of void ordering observations in irradiated BCC and FCC metals^a

Metal	Irradiation conditions	Void density $\times 10^{-23}$ (m^{-3})	Void diameter (nm)	Superlattice parameter, λ (nm)
Mo [17]	2 MeV N+; 870°C; 100 dpa	2.0	4.0	22.0
Mo [66, 111]	7.5 MeV Ta+; 900°C; 130 dpa		6.0	31.0
Mo [111]	Fission neutrons; 585°C; 10 dpa	0.16	6.2	46.0
	7.5 MeV Ta+; 900°C; 150 dpa	0.16	15	46.0
Mo [30]	Fission neutrons; 450°C; 36 dpa	0.72	6.4	26.5
	7.5 MeV Ta+; 790°C; 36 dpa	0.54	7.2	32.8
Mo [111]	7.5 MeV Ta+; 450°C; 7.5 dpa	2.8	≈ 2.5	22.0
	7.5 MeV Ta+; 450°C; 18 dpa	1.3	4.5	22.0
	7.5 MeV Ta+; 450°C; 40 dpa	0.35	≈ 4.0	22.0
	7.5 MeV Ta+; 600°C; 40 dpa	1.1	5.4	28.0
	7.5 MeV Ta+; 715°C; 40 dpa	0.85	5.7	32.8
	7.5 MeV Ta+; 900°C; 40 dpa	0.5	5.8	37.0
Mo [115]	Fission neutrons; 430°C; 5 dpa			21.0
	Fission neutrons; 580°C; 5 dpa			27.0
	Fission neutrons; 680°C; 5 dpa			30.5
	Fission neutrons; 800°C; 5 dpa			40.0
	Fission neutrons; 900°C; 5 dpa			47.0
	Fission neutrons; 1050°C; 5 dpa			66.0
Mo-0.5%Ti [17] -0.1%Zr	2 MeV N+; 870°C; 300 dpa		<6	22.0
Mo-0.5%Ti [30]	Fission neutrons; 585°C; 36 dpa	2.4	6.9	21.5
	Fission neutrons; 790°C; 36 dpa	0.6	7.2	31.5
W [115]	Fission neutrons; 580°C; 2 dpa		3.0	19.5
	Fission neutrons; 680°C; 2 dpa		–	20.0
	Fission neutrons; 800°C; 2 dpa		–	21.0
	Fission neutrons; 900°C; 2 dpa		4.0	25.0
	Fission neutrons; 1050°C; 2 dpa		–	30.0
Nb [29]	5 MeV Ni+; 800°C; 5 dpa	0.2	4.5	35.0
Nb [17]	7.5 MeV Ta+; 800°C; 140 dpa		12.5	34.0
	7.5 MeV Ta+; 800°C; 290 dpa		11.0	38.0
	7.5 MeV Ta+; 900°C; 300 dpa		25.0	75.0
Nb and Nb-1%Zr [116]	3.2 MeV Ni or V+; 650°C; 30-140 dpa		1.6	10.0
	3.2 MeV Ni or V+; 780°C; 30-140 dpa		7.5	25.0
	3.2 MeV Ni or V+; 805°C; 30-140 dpa		14.0	35.0
	3.2 MeV Ni or V+; 850°C; 30-140 dpa		10.0	34.0
	3.2 MeV Ni or V+; 925°C; 30-140 dpa		25.0	61.0
	3.2 MeV Ni or V+; 1010°C; 30-140 dpa		78.0	145.0
Nb [30]	Fission neutrons; 790°C; 34 dpa	0.028	18.6	66.5
Ta [30]	Fission neutrons; 585°C; 36 dpa	1.9	6.1	20.5
Ni [66, 29]	5 MeV Ni+; 525°C; 360-480 dpa	0.41	25.0	62.0
	6 MeV Se+; 525°C; 400 dpa	0.14	18.0	66.0
Ni-2%Al [117]	0.4 MeV N+; 500°C; 70 dpa	0.14	14.0	65.0

^aImperfect (partially ordered) void lattices also been reported for irradiated Al [118, 119, 120], Ni-Al alloys [117], stainless steel [121] and Cu-10%Ni [122].

Table 3. Summary of gas bubble ordering observations in irradiated BCC and FCC metals^a

Metal	Irradiation conditions	Bubble density $\times 10^{-25}$ (m ⁻³)	Bubble diameter (nm)	Superlattice parameter, λ (nm)
Mo [23, 112, 113]	36 keV He+; 25°C; 1×10^{21} m ⁻²	1.4	2.4	5.2
	36 keV He+; 700°C; 2×10^{21} m ⁻²	1.6	2.4	5.0
	40 keV He+; 500°C; 5×10^{21} m ⁻²	1.3	2.4	5.4
Mo [113]	40-60 keV He+; 400°C; 8×10^{21} m ⁻²	0.8	2.2	6.2
Mo [112]	100 keV Ne+; 550°C; 1×10^{21} m ⁻²	1.5		5.1
Cr [113]	40 keV He+; 25°C; 3×10^{21} m ⁻²	1.5	2.4	5.1
W [113]	50 keV He+; 500°C; 1.5×10^{21} m ⁻²	0.8	2.0	6.2
V [113]	30 keV He+; 50°C; 5×10^{21} m ⁻²	3.4	1.5	3.9
Ta [113]	30 keV He+; 300°C; 5×10^{21} m ⁻²	0.8	2.3	6.4
Fe [113]	50 keV He+; 25°C; 3×10^{21} m ⁻²	0.8	2.5	6.0
Cu [113, 125]	30 keV He+; 25°C; 4×10^{21} m ⁻²	1.0	2.0	7.6
Cu [125]	16 keV H+; 25°C; 1.3×10^{23} m ⁻²	0.2	2	12
Au [126]	160 keV He+; 5°C; 1×10^{22} m ⁻²		2	8
Ni [125]	30 keV He+; 25°C; 4×10^{21} m ⁻²	1.4	2	6.6
Ni [127]	0.25-8 keV He+; 25°C; 1×10^{21} m ⁻²		2	8.1
316 SS [125]	30 keV He+; 25°C; 4×10^{21} m ⁻²	1.5	2	6.5
321 SS [125]	30 keV He+; 25°C; 4×10^{21} m ⁻²	1.5	2	6.4

^aThe {110} interplanar spacing for the bubble lattice originally reported in [23, 112] has been converted to the appropriate BCC superlattice parameter [113].

is the production rate of freely-migrating point defects. These defects diffuse with diffusion coefficients D_r , undergo recombination at a rate $\alpha c_1 c_2$ and are absorbed at microstructural defects $\{q\}$ (network dislocations, vacancy and interstitial loops, voids, etc.). The capture rate at microstructural defects is proportional to their sink strength ρ_q (e.g., for dislocation sinks it is the density, while in the case of voids it is $\rho_1 = 4\pi N_1 r_1$, where N_1 is the number density and r_1 the mean radius). Z_{qr} are absorption bias and Φ_{qr} are thermal emission rates of point defects from microstructures. One may generally assume that vacancy bias factors are defined, such that $Z_{q1} = 1$ and that interstitial bias are such that $Z_{q2} = 1 + B$, except for voids, since $Z_{12} \simeq 1$. On the other hand, Q_q is the volume fraction occupied by the microstructural defect q (e.g., for voids, $Q_1 = 4\pi N_1 r_1^3 / 3$), and $\epsilon_q P$ is its creation rate from cascades.

Homogeneous solutions of the equation set (1) satisfy some useful conservation equations. For example,

$$\dot{c}_2 - \dot{c}_1 = \Sigma_q \dot{Q}_q. \quad (2)$$

Another simplifying element is that point defect evolution is so fast that their concentration adjusts itself on microstructural sink densities. c_r may thus be adiabatically eliminated from the dynamics and explicit expressions for \dot{Q}_q may be obtained in two well known approximations, namely the sink dominant case, where loss of point defects to sinks dominates loss due to pair annihilation, and the recombination limit, where pair annihilation is dominant. Linear stability analysis of the resulting uniform solutions may then be performed. A linear evolution matrix is derived for the Fourier modes of small perturbations of uniform solutions,

in a quasi steady state approximation. If only one eigenvalue of this evolution matrix becomes positive, the reference state is unstable, since the corresponding eigenmode starts growing. If the unstable eigenvalue is real and if the instability occurs for nonzero wavenumbers, one has a spatial instability, which usually leads to the development of stationary spatial patterns. Such an instability is easily obtained, in this model, provided that the interaction bias, B , is sufficiently large versus the cascade collapse efficiency ϵ_2 (when only vacancy cascades are considered).

Krishan's analysis [51, 54, 59] essentially shows that the three basic elements that lead to spatial instability of microstructural defect densities originate in point defect dynamics. These are: production bias (differences in point defect production rates), interaction bias (differences in capture rates at microstructural defects) and appropriate couplings between sinks and point defects. This analysis has been limited to the determination of instability conditions. It is thus only able to describe the early stages of nano- and microstructure formation. It shows, for example, that the emerging wavelength is inversely proportional to the square root of the sink strength. However, the determination of the fully developed ordered structures, which requires at least a weakly nonlinear analysis beyond the instability, has not been addressed in this discussion, and needs an examination of the post-bifurcation behavior of the unstable solutions.

4.2. VACANCY CLUSTER PATTERNING

The approach outlined in the preceding section has been applied by Murphy to the special case of vacancy loop ordering under irradiation in the absence of voids [56]. Following Bullough, Eyre and Krishan [128], Murphy described the coupled evolution of point defects and vacancy loops in the framework of a one-dimensional rate theory dynamical model. In this description, point defects are the only mobile species, which diffuse in space. They may annihilate by recombination or through absorption by network dislocations and vacancy loops, which are immobile and are supposed to be created instantaneously by cascade effects.

$$\begin{aligned}
 \partial_t c_i &= P - \alpha c_i c_v + D_i \partial_x^2 c_i - D_i c_i (Z_{iN} \rho_N + Z_{iV} \rho_V), \\
 \partial_t c_v &= P(1 - \epsilon) - \alpha c_i c_v + D_v \partial_x^2 c_v - \\
 &\quad - D_v (Z_{vN} (c_v - \bar{c}_{vN}) \rho_N + Z_{vV} (c_v - \bar{c}_{vV}) \rho_V), \\
 \partial_t \rho_V &= \frac{1}{|\mathbf{b}| r_V^0} [\epsilon P - \rho_V (D_i Z_{iV} c_i - D_v Z_{vV} (c_v - \bar{c}_{vV}))],
 \end{aligned} \tag{3}$$

where P is the displacement damage rate of point defects, ϵ the cascade collapse efficiency, responsible for the trapping of part of the vacancies in dislocation loops. ρ_N is the line density of network dislocations and ρ_V is the line density of vacancy loops, given by $\rho_V = 2\pi r_V N_V$, where r_V and N_V are the mean radius and number density of loops, respectively. The mean loop radius is approximately constant and equal to $r_V^0/2$, where r_V^0 is the initial loop radius. \mathbf{b} is the Burgers vector and $Z_{vr} \simeq 1$ and $Z_{ir} \simeq 1 + B$. Furthermore, the network dislocation density is assumed to be uniform and constant in time.

The system (3) admits uniform steady state solutions c_i^0 , c_v^0 and ρ_V^0 . Their linear stability analysis has been performed on defining the spatial fluctuations of defect densities through $c_r(x, t) = c_r^0(1 + \bar{c}_r(x, t))$ and $\rho_V(x, t) = \rho_V^0(1 + \bar{\rho}_V(x, t))$ [56]. The linear evolution matrix for a Fourier mode of wavenumber k of these fluctuations is given by:

$$\mathbf{M} = \begin{pmatrix} -\bar{P}/c_v^0 - k^2 D_v & -\alpha c_i^0 & -D_v Z_{vV}(c_v^0 - \bar{c}_{vV})\rho_v^0/c_v^0 \\ -\alpha c_v^0 & -P/c_i^0 - k^2 D_i & -D_i Z_{iV}\rho_v^0 \\ \frac{D_v Z_{vV}c_v^0}{|\mathbf{b}|r_v^0} & -\frac{D_i Z_{iV}c_i^0}{|\mathbf{b}|r_v^0} & -\frac{\epsilon P}{|\mathbf{b}|r_v^0\rho_v^0} \end{pmatrix}, \quad (4)$$

where $\bar{P} = P(1 - \epsilon) + D_v(Z_{vN}\rho_N\bar{c}_{vN} + Z_{iV}\rho_v^0\bar{c}_{vV})$.

If at least one eigenvalue of this matrix has positive real part at finite k , the corresponding eigenmode will grow and destabilize uniform solutions by giving rise to spatial oscillations. Determination of the eigenvalues of this matrix requires the solution of a cubic characteristic equation. However, since the response of vacancy and interstitial densities to small perturbations are much more rapid than the response of vacancy loop densities, this characteristic equation may be reduced to a form giving the growth rate of linear perturbations.

This linear growth rate has been computed numerically [56] for parameter values corresponding to 316 stainless steel [52]. It has been found positive for wavelengths in the micron range and network dislocation densities lower than some critical value. An interesting aspect of this analysis is also the temperature dependence of the wavelength of the fastest growing perturbations. For network dislocation densities in the range $10^{12} - 10^{13} \text{ m}^{-2}$, this wavelength increases slightly with temperature below $500 \text{ }^\circ\text{C}$, and then strongly at higher temperatures [56]. It may also be shown that the wavelength decreases with increasing displacement rate. Similar calculations have also been made for neutron-irradiated copper at $250 \text{ }^\circ\text{C}$, where, for a network dislocation density of 10^{11} m^{-2} , instability was found for a wavelength of approximately $0.34 \text{ } \mu\text{m}$, which is several times larger than typical experimental observations [55]. This discrepancy will be explained later to be a result of non-linear interactions between unstable modes. Hence, it has been shown here that the simplified rate theory is able to provide qualitative predictions of an instability in the dislocation structure of irradiated materials. However, in this simplified model, only vacancy loop density was considered as the only microstructural defect able to vary spatially in a one-dimensional geometry. Furthermore, the problem of the saturation of the instability and of the characterization of the final pattern has not been addressed in this work, and will be addressed in greater detail in the next section.

5. Nonlinear dynamics of nano-structure evolution

From the results outlined in the preceding section, it appears that the rate theory may provide the right tools for a coherent description of nano- and microstructure formation under irradiation. However, in order to achieve a complete understanding of the selection mechanisms of defect microstructure, a more complete analysis, especially of the post-bifurcation regime is needed. In a series of papers by Walgraef and Ghoniem [61–63], reaction-diffusion models for coupled evolution of various defects involved in microstructure formation were constructed and analyzed from the point of view of nonlinear dynamics and pattern formation theory. They first considered point and line defects only, and emphasized the spatial ordering of vacancy loops. Then, in order to describe microstructure formation and evolution in general, they extended the dynamical model to include volume defects such as voids or stacking fault tetrahedra, and discussed how the presence of such defects could affect nano- and microstructure evolution. The influence of anisotropic SIA diffusion on the spatial symmetry of self-organized nano- and microstructure was also analyzed. They showed how different mobil-

ities and production/absorption asymmetries (bias) of point defects could trigger instabilities in uniform defect distributions and induce the formation of defect nano- and microstructure. The selection and stability of the corresponding spatial structures could be studied, in the post-bifurcation regime, by weakly nonlinear analytical methods and full numerical analysis [63]. Hence, we will review here this more complete formulation, and discuss the results in relation to available experimental observations.

5.1. THE DYNAMICAL MODEL

Let us consider the model introduced in [63], which is based on the evolution of interacting point, line and volume defects. We will first discuss the structure of the kinetic equations for each type of defect.

Point defect kinetic equations

$$\begin{aligned}\partial_t c_i &= P(1 - \epsilon_i) - \alpha c_i c_v + D_i \nabla^2 c_i - D_i c_i (Z_{iN} \rho_N + Z_{iV} \rho_V + Z_{iI} \rho_I + Z_{iC} \rho_C), \\ \partial_t c_v &= P(1 - \epsilon_v) - \alpha c_i c_v + D_v \nabla^2 c_v - D_v (Z_{vN} (c_v - \bar{c}_{vN}) \rho_N - \\ &\quad + Z_{vV} (c_v - \bar{c}_{vV}) \rho_V + Z_{vI} (c_v - \bar{c}_{vI}) \rho_I + Z_{vC} (c_v - \bar{c}_{vC}) \rho_C),\end{aligned}\quad (5)$$

where the notation is similar to the one used in [56]: c_v corresponds to the concentration of vacancies and c_i to interstitials. ρ_N is the network dislocation density, ρ_V the vacancy loop density, ρ_I the interstitial loop density and ρ_C the void sink density ($\rho_C = 4\pi N_c R_c$ with N_c being the void number density and R_c the mean void radius). P is the displacement damage rate, $\epsilon_i P$ the in-cascade interstitial loop production rate and ϵ_v the cascade collapse efficiency of vacancy loops, α is the recombination coefficient, \mathbf{b} the Burgers vector, r_V^0 the mean vacancy loop radius and Z_{\dots} are the bias factors (which may usually be approximated by $Z_{iN} = Z_{iI} = Z_{iV} = 1 + B$ and $Z_{vI} = Z_{vN} = Z_{vV} = Z_{vC} = Z_{iC} = 1$, B being the excess network bias). \bar{c}_{vN} , \bar{c}_{vV} , \bar{c}_{vI} and \bar{c}_{vC} are the concentrations of thermally emitted vacancies from network dislocations, vacancy and interstitial loops, and voids, respectively.

The basic processes responsible for defect density evolution are easily identified in Eq. (5). Their net production rate results from the balance between displacement damage rate, responsible for the generation of Frenkel pairs, and loop production rates. Vacancy and interstitial loops are assumed to be produced by cascades, and their production rate is proportional to the corresponding cascade collapse efficiency, which introduces a production bias in rate equations. Note that this production bias is considered to be an important element in modeling of void swelling [129, 130]. Point defects are annihilated through pair recombination or absorption at line (dislocations and loops) or surface (voids or bubbles) defects. The sink strength for point defect absorption are $Z_{i\chi} \rho_\chi$ and $Z_{v\chi} \rho_\chi$, for interstitials and vacancies respectively (χ representing the type of line or volume defect). The difference between $Z_{i\chi}$ and $Z_{v\chi}$ (B , in this model) introduces a second asymmetry in defect evolution, which is usually referred to as the absorption bias. Therefore, two types of asymmetries are involved in determining point defect balance: (1) productions rates of free point defects; (2) absorption rates at biased sinks (i.e., components of the dislocation microstructure).

Kinetic equations for dislocation loops

In this description, the network dislocation density is considered as uniform and constant in time, and one has to consider the evolution of vacancy and interstitial loop densities only:

$$\begin{aligned}\partial_t \rho_l &= \left(\frac{2\pi N}{|\mathbf{b}|} \right) (\epsilon_i P + D_i Z_{iI} c_i - D_v Z_{vI} (c_v - \bar{c}_{vI})), \\ \partial_t \rho_v &= \frac{1}{|\mathbf{b}| r_V^0} [\epsilon_v P - \rho_v (D_i Z_{iV} c_i - D_v Z_{vV} (c_v - \bar{c}_{vV}))]\end{aligned}\quad (6)$$

The basic elements of line defect density evolution are thus creation through cascades and growth or shrinking processes caused by point defect absorption. These defects are considered as immobile, although SIA may also form glissile clusters (i.e., small interstitial loops), which may play an important role in void swelling and ordering [131]

Kinetic equations for void evolution

In this review, the only volume defects we will consider are voids. If one may consider that they have spherical shapes and a mean radius R_c , the radius evolution is determined by the balance between the point defect fluxes, and is given by

$$\partial_t R_c = \frac{1}{R_c} [D_v Z_{vC} (c_v - \bar{c}_{vC}) - D_i Z_{iC} c_i]. \quad (7)$$

Beyond the nucleation period, the void number density N_c may be treated as a constant. The evolution of the sink density, $\rho_c = 4\pi N_c R_c$, is thus given by

$$\partial_t \rho_c = \frac{(4\pi N_c)^2}{\rho_c} [D_v Z_{vC} (c_v - \bar{c}_{vC}) - D_i Z_{iC} c_i] \quad (8)$$

and for the void swelling rate, $S = \frac{4\pi}{3} R_c^3 N_c$, one has

$$\partial_t S = [D_v Z_{vC} (c_v - \bar{c}_{vC}) - D_i Z_{iC} c_i] \rho_c. \quad (9)$$

Scaled variables

The complete model (5, 6, 8) may be simplified by introducing the following scaling relations:

$$\begin{aligned}\lambda_v &= D_v Z_{vN} \rho_N, & \bar{D} &= D / \lambda_v, & \alpha / \lambda_v &= \gamma, & P &= \gamma P / \lambda_v, \\ \rho_{v,I}^* &= \frac{\rho_{v,I}}{\rho_N}, & x_{i,v} &= \gamma c_{i,v}, & \bar{x}_{vN} &\ll \bar{x}_{vV} \simeq \bar{x}_{vI} \simeq \bar{x}_{vC} = \bar{x}_{vL}, \\ \mu &= \frac{D_i}{D_v}, & \tau &= \lambda_v t, \\ \tau_I &= \frac{b\alpha\rho_N}{2\pi N D_v}, & \tau_V &= b r_v^0 \rho_N \gamma, & \tau_C &= \frac{\alpha \rho_N^2}{(4\pi N_c)^2 D_v}.\end{aligned}\quad (10)$$

The complete system of kinetic equations may then be written in dimensionless form:

$$\begin{aligned}\partial_\tau x_i &= P(1 - \epsilon_i) - x_i x_v + \mu \bar{D}_v \nabla^2 x_i - \mu x_i ((1 + B)(1 + \rho_v^* + \rho_l^*) + \rho_c^*), \\ \partial_\tau x_v &= P(1 - \epsilon_v) - \bar{x}_{vL} - x_i x_v + \bar{D}_v \nabla^2 x_v - (x_v - \bar{x}_{vL})(1 + \rho_v^* + \rho_l^* + \rho_c^*), \\ \tau_I \partial_\tau \rho_l^* &= \epsilon_i P + \mu(1 + B)x_i - (x_v - \bar{x}_{vL}), \\ \tau_V \partial_\tau \rho_v^* &= \epsilon_v P - \rho_v^* (\mu(1 + B)x_i - (x_v - \bar{x}_{vL})), \\ \tau_C \partial_\tau \rho_c &= \frac{1}{\rho_c^*} [(x_v - \bar{x}_{vL}) - \mu x_i].\end{aligned}\quad (11)$$

5.2. DISLOCATION AND VOID DYNAMICS

As already mentioned earlier, point defect densities evolve much more rapidly than that of loops. They may be adiabatically eliminated from the dynamics and their actual values may be expressed as functions of loop densities [63]. In the case of uniform defect densities, the instability in the uniform defect population is attained when point defect recombination is negligible (i.e., in the sink dominated regime [63]). Point defect recombination is unimportant when the following condition applies [132]:

$$4\alpha P < \lambda_i \lambda_v \quad (12)$$

Point defect concentrations are thus given by:

$$\begin{aligned} (x_v^0 - \bar{x}_{vL}) &= \frac{P(1 - \epsilon_v) - \Delta}{A_0} \\ x_i^0 &= \frac{P(1 - \epsilon_i)}{\mu(1 + B)B_0} \end{aligned} \quad (13)$$

where $\Delta = \bar{x}_{vL} - \bar{x}_{vN} \simeq \bar{x}_{vL}$, $A_0 = 1 + \rho_V^0 + \rho_I^0 + \rho_C^0$ and $B_0 = 1 + \rho_V^0 + \rho_I^0 + \frac{\rho_C^0}{1+B}$.

In the case of inhomogeneous defect densities, point defect perturbations may be expressed as an expansion in powers of the loop density perturbations, and their Fourier transform may be written, in vectorial form, as [63]:

$$\delta \mathbf{x}_{\mathbf{q}} = \sum_{n \geq 1} \int d\mathbf{k} \dots \int d\mathbf{k}_{n-1} (-1)^{(n)} \mathbf{D}_{\mathbf{q}, \dots, \mathbf{k}_{n-1}}^{(n)} \mathbf{T}_{\mathbf{q}} \delta \rho_{\mathbf{q}-\mathbf{k}} \dots \delta \rho_{\mathbf{k}_{n-1}} \quad (14)$$

where

$$\delta \mathbf{x}_{\mathbf{q}} = \begin{pmatrix} \delta x_{i,\mathbf{q}} \\ \delta x_{v,\mathbf{q}} \end{pmatrix}, \quad (15)$$

$$\mathbf{T}_{\mathbf{q}} = \begin{pmatrix} \frac{P(1 - \epsilon_i)}{\mu(1 + B)B_0} \\ \frac{P(1 - \epsilon_v) - \Delta}{A_0} \end{pmatrix}, \quad (16)$$

$$\mathbf{D}_{\mathbf{q}, \dots, \mathbf{k}_{n-1}}^{(n)} = \begin{pmatrix} \frac{1}{B_q \dots B_{k_{n-1}}} & 0 \\ 0 & \frac{1}{A_q \dots A_{k_{n-1}}} \end{pmatrix} \quad (17)$$

and

$$\delta \rho_{\mathbf{q}} = \rho^0 \delta \rho_{\mathbf{q}}, \quad (18)$$

with

$$\rho^0 = \begin{pmatrix} \rho_V^0 & \rho_I^0 & \frac{\rho_C^0}{1+B} \\ \rho_V^0 & \rho_I^0 & \rho_C^0 \end{pmatrix} \quad (19)$$

and

$$\delta\rho_{\mathbf{q}} = \begin{pmatrix} \delta\rho_{V_{\mathbf{q}}} \\ \delta\rho_{I_{\mathbf{q}}} \\ \delta\rho_{C_{\mathbf{q}}} \end{pmatrix}. \quad (20)$$

Furthermore, $B_{\mathbf{q}} = B_0 + q^2 \bar{D}_v / 1 + B$, $A_{\mathbf{q}} = A_0 + q^2 \bar{D}_v$ and

$$\begin{aligned} \delta x_i &= x_i - x_i^0, & \delta x_v &= x_v - (x_v^0 - \bar{x}_{vL}), \\ \delta\rho_v &= \frac{\rho_v^* - \rho_v^0}{\rho_v^0}, & \delta\rho_i &= \frac{\rho_i^* - \rho_i^0}{\rho_i^0}, & \delta\rho_c &= \frac{\rho_c^* - \rho_c^0}{\rho_c^0}, \end{aligned} \quad (21)$$

where x_i^0 , x_v^0 , ρ_v^0 , ρ_i^0 and ρ_c^0 are the uniform defect densities.

This adiabatic elimination of point defect densities leads to a reduction to the dynamics of dislocation loops and void densities, which govern the evolution of the whole system. The reduced kinetic equations for uniform defect densities are:

$$\begin{aligned} \tau_I \partial_\tau \rho_i^0 &= \epsilon_i P + \frac{P(1 - \epsilon_i)}{B_0} - \frac{P(1 - \epsilon_v) - \Delta}{A_0}, \\ \tau_V \partial_\tau \rho_v^0 &= \epsilon_v P - \left[\frac{P(1 - \epsilon_i)}{B_0} - \frac{P(1 - \epsilon_v) - \Delta}{A_0} \right] \rho_v^0, \\ \tau_C \partial_\tau \rho_c^0 &= -\frac{1}{\rho_c^0} \left[\frac{P(1 - \epsilon_i)}{(1 + B)B_0} - \frac{P(1 - \epsilon_v) - \Delta}{A_0} \right] \end{aligned} \quad (22)$$

and the evolution equations of nonuniform loop densities may be cast in the following vectorial form :

$$\tau \partial_\tau \delta\rho_{\mathbf{q}} = \mathbf{L} \delta\rho_{\mathbf{q}} + \mathbf{M} \delta\mathbf{x}_{\mathbf{q}} + \int d\mathbf{k} \delta\rho_{\mathbf{q}-\mathbf{k}} \mathbf{N} \delta\mathbf{x}_{\mathbf{k}} + \int d\mathbf{k} \delta\rho_{\mathbf{q}-\mathbf{k}} \mathbf{P} \delta\rho_{\mathbf{q}-\mathbf{k}} + \dots, \quad (23)$$

where

$$\tau = \begin{pmatrix} \tau_V & 0 & 0 \\ 0 & \tau_I & 0 \\ 0 & 0 & \tau_C \end{pmatrix}, \quad (24)$$

$$\mathbf{L} = \begin{pmatrix} -\frac{\epsilon_v P}{\rho_v^0} & 0 & 0 \\ 0 & -\frac{(\epsilon_i P + \Gamma)}{\rho_i^0} & 0 \\ 0 & 0 & \frac{2}{\rho_c^{02}} \bar{\Gamma} \end{pmatrix}, \quad (25)$$

$$\mathbf{M} = \begin{pmatrix} -\mu(1 + B) & 1 \\ \frac{\mu(1 + B)}{\rho_i^0} & -\frac{1}{\rho_i^0} \\ -\frac{\mu}{\rho_c^{02}} & \frac{1}{\rho_c^{02}} \end{pmatrix}, \quad (26)$$

$$\mathbf{N} = \begin{pmatrix} -\mu(1+B) & 1 \\ 0 & 0 \\ \frac{\mu}{\rho_c^{02}} & -\frac{1}{\rho_c^{02}} \end{pmatrix} \quad (27)$$

and

$$\mathbf{P} = \begin{pmatrix} 0 & 0 & 0 \\ 0 & 0 & 0 \\ 0 & 0 & -\frac{\bar{\Gamma}}{\rho_c^{02}} \end{pmatrix} \quad (28)$$

with

$$\Gamma = \frac{P(1-\epsilon_i)}{B_0} - \frac{P(1-\epsilon_v) - \Delta}{A_0},$$

$$\bar{\Gamma} = \frac{P(1-\epsilon_i)}{(1+B)B_0} - \frac{P(1-\epsilon_v) - \Delta}{A_0}$$

$$\bar{\epsilon} = \epsilon_v - \epsilon_i$$

and supplemented with Eqs. (14).

5.3. THE ONSET OF SPATIAL INSTABILITY

In order to determine the possible development of spatial instability in the system, one has to know, in the first place, the evolution of the uniform loop and void defect densities, which may be evaluated through Eqs. (14) and (23).

Consider first the growth rate of the void density. It is easy to see that, when the net contribution of interstitials to the void growth rate exceeds the net contribution of vacancies to the void growth rate, or

$$\frac{P(1-\epsilon_i)}{(1+B)} > (P(1-\epsilon_v) - \Delta), \quad (29)$$

or $\epsilon_v - \epsilon_i + (\Delta/P) \geq B$, so that the production bias is larger than the absorption bias, the void growth continuously decreases, and will not affect the long time behavior of the system. This corresponds to the shrinkage regime already discussed by Krishan [59]. In this case, the asymptotic kinetic microstructure behavior is restricted to the evolution of dislocation loops only. Of course, due to the weak coupling between the concentrations of loops and voids, any spatial instability in loop densities will eventually induce transient structures in the void density. This condition is consistent with the experimental condition of irradiation at low temperature (less than one-third of the melting point).

On the other hand, under conditions conducive of void growth (temperatures above one third of the melting point), one has:

$$\frac{P(1-\epsilon_i)}{(1+B)} < (P(1-\epsilon_v) - \Delta), \quad (30)$$

In this case, the situation is quite different, since dimensional analysis of the evolution Eqs.(22) shows that both loop and void densities increase with time or irradiation dose.

The stability of uniform dislocation densities may be analyzed through the linear part of the evolution equation for their inhomogeneous perturbations. This evolution is obtained by combining Eqs. (14) and (23). Its linear part reads :

$$\tau \partial_t \delta \rho_q = [\mathbf{L} - \mathbf{M} \mathbf{D}_q \mathbf{T}_q \rho^0] \delta \rho_q = \Omega_q \delta \rho_q \quad (31)$$

where

$$\Omega_q = \begin{pmatrix} -\frac{\epsilon_v P}{\rho_v^0} + \Lambda_q \rho_v^0 & \Lambda_q \rho_l^0 & \bar{\Lambda}_q \rho_c^0 \\ -\Lambda_q \frac{\rho_v^0}{\rho_l^0} & -\frac{(\epsilon_i P + \Gamma)}{\rho_l^0} - \Lambda_q & -\bar{\Lambda}_q \frac{\rho_c^0}{\rho_l^0} \\ \bar{\Lambda}_q \frac{\rho_v^0}{\rho_c^{02}} & \bar{\Lambda}_q \frac{\rho_l^0}{\rho_c^{02}} & \frac{2}{\rho_c^{02}} \bar{\Gamma} + \bar{\bar{\Lambda}}_q \frac{1}{\rho_c^0} \end{pmatrix}, \quad (32)$$

where

$$\Lambda_q = \frac{P(1 - \epsilon_i)}{B_0 B_q} - \frac{P(1 - \epsilon_v) - \Delta}{A_0 A_q}, \quad (33)$$

$$\bar{\Lambda}_q = \frac{P(1 - \epsilon_i)}{(1 + B) B_0 B_q} - \frac{P(1 - \epsilon_v) - \Delta}{A_0 A_q}, \quad (34)$$

$$\bar{\bar{\Lambda}}_q = \frac{P(1 - \epsilon_i)}{(1 + B)^2 B_0 B_q} - \frac{P(1 - \epsilon_v) - \Delta}{A_0 A_q}. \quad (35)$$

Since the elements of the corresponding evolution matrix are time-dependent, this situation does not generally allow performing the usual stability analysis. Nevertheless, some insight into the behavior of the system may be obtained within a quasi-static approximation. In this description, the time (or irradiation dose) appears just as a parameter, and one may obtain an instantaneous instability criterion. When at least one eigenvalue of the evolution matrix acquires a positive real part, the corresponding eigenmode starts growing. Of course this approximation does not describe correctly the time evolution of perturbations, but it seems to predict the instability threshold quite accurately in similar problems.

In fact, one may show [63] that nonuniform defect densities start growing when the fraction of line defects corresponding to vacancy loops exceeds an instability threshold given, at the lowest order in ϵ_v , ϵ_i , B , Δ , by:

$$b = \frac{\rho_v^0}{1 + \rho_l^0 + \rho_v^0} > b_c = \frac{\rho_v^0}{1 + \rho_l^0 + \rho_v^0} \Big|_c = \frac{2\sqrt{\epsilon_v B}}{B + \bar{\epsilon} + \frac{B}{1 + B} \frac{\rho_c^0}{A_0}} \quad (36)$$

where $\bar{\epsilon} = \epsilon_v - \epsilon_i + \Delta/P$.

This instability occurs for a critical wavenumber given by:

$$q_c^2 = \frac{(1 + \rho_l^0 + \rho_v^0)(B - \bar{\epsilon}) - \rho_c^0(2B + \bar{\epsilon})}{\bar{D}_v(B + \bar{\epsilon} + \frac{B}{1 + B} \frac{\rho_c^0}{A_0})}. \quad (37)$$

One immediately sees that one recovers already known qualitative results, namely that network dislocations tend to stabilize uniform distributions, and that the critical wavelength decreases for increasing network dislocation density. Furthermore, the instability threshold also decreases for increasing void density, and occurs at finite q_c , when the following condition is satisfied:

$$\frac{\rho_c^0}{1 + \rho_l^0 + \rho_v^0} < \frac{B - \bar{\epsilon}}{2B + \bar{\epsilon}}, \quad (38)$$

which implies that self-organized nano- and microstructure formation occurs when the absorption bias exceeds the production bias, and the uniform void density does not exceed a well defined fraction of the total line defect density. Furthermore, for all materials parameters fixed, one sees that an increase of defect densities (voids or dislocations) tends to decrease the wavelength of the critical microstructure.

5.4. PATTERN SELECTION IN THE WEAKLY NON-LINEAR REGIME

It is well-known that linear analysis is not sufficient to determine what type of nano- and microstructure is selected beyond the instability. Pattern selection and stability are determined by nonlinear criteria, and requires thus nonlinear analysis [64]. Fortunately, close to the instability threshold of the steady uniform reference state of a nonlinear dynamical system, space-time separation occurs between stable and unstable modes, the characteristic scales of the latter being by far the largest. The stable modes may thus be adiabatically eliminated, and the dynamics reduced to the weakly nonlinear unstable mode dynamics, which governs the long time evolution of the system and captures the asymptotic properties of the complete kinetic model in the vicinity of its bifurcation point. When this adiabatic elimination is performed, one usually obtains amplitude equations for the bifurcating solutions which have the structure of Landau or Landau–Ginzburg equations, and which have been discussed and analyzed at length in the literature in relation to the development of spatio-temporal patterns and self-organization phenomena in numerous non-equilibrium physico-chemical systems [4, 64].

In the present case, the uniform reference state is time evolving, and one cannot generally perform this type of analysis. However, for weak nonlinearities, the void and loop dynamics can still be expressed as an expansion in the defect densities. Using Eqs. (14) and (23), one obtains:

$$\tau \partial_\tau \delta \rho_q = \Omega_q \delta \rho_q + \int dk \mathcal{V}_{\mathbf{q}, \mathbf{k}} \delta \rho_{q-k} \delta \rho_k + \int dk \int dk_1 \mathcal{U}_{\mathbf{q}, \mathbf{k}, \mathbf{k}_1} \delta \rho_{q-k} \delta \rho_{k-k_1} \delta \rho_{k_1}, \quad (39)$$

where

$$\mathcal{V}_{\mathbf{q}, \mathbf{k}} = \mathbf{M} \mathbf{D}_{q, k}^{(2)} \mathbf{T}_q (\rho^0)^2 - \mathbf{N} \mathbf{D}_q \mathbf{T}_q \rho^0 + \mathbf{P} \quad (40)$$

and

$$\mathcal{U}_{\mathbf{q}, \mathbf{k}, \mathbf{k}_1} = -\mathbf{M} \mathbf{D}_{q, k, k_1}^{(3)} \mathbf{T}_q (\rho^0)^3 + \mathbf{N} \mathbf{D}_{q, k}^{(2)} \mathbf{T}_q (\rho^0)^2. \quad (41)$$

Except in the quasi-static approximation, the usual procedure of diagonalization of the linear evolution matrix and adiabatic elimination of stable modes may not be performed on this dynamical system, due to the time-dependence of the coefficients. However, since $\tau_C \gg \tau_l \gg \tau_v$, and since the elements of the matrices \mathbf{M} and \mathbf{N} are such that their lower components

decrease with time (or dose), it is easy to see from dimensional analysis, that the dynamics is driven by the vacancy loops. For weak deviations from the uniform density, and at leading order in $\epsilon = (b - b_c)/b_c$, and $(q - q_c)/q_c$, the vacancy loop density perturbation in Fourier space can then be expressed as:

$$\tau_0 \partial_\tau \delta \rho_{Vq} = \omega_q \delta \rho_{Vq} + \int dk v_{q_c} \delta \rho_{Vq-k} \delta \rho_{Vk} + \int dk \int dk_1 u_{q_c} \delta \rho_{Vq-k} \delta \rho_{Vk-k_1} \delta \rho_{Vk_1}, \quad (42)$$

where

$$\omega_q = \frac{b - b_c}{b_c} - \xi_0^2 \left(\frac{q^2 - q_c^2}{q_c^2} \right)^2, \quad (43)$$

$$\tau_0 = \tau_V \bar{\tau} = \frac{2\tau_V}{\sqrt{B\epsilon_v}(B + \bar{\epsilon})}, \quad (44)$$

$$v_{q_c} = \frac{\epsilon_v P \bar{\tau}}{\rho_v^0} + O\left(\frac{1}{A_0^2}\right), \quad (45)$$

$$u_{q_c} = \left(\frac{P(1 - \epsilon_v) - \Delta}{A_0 A_{q_c}^2} - \frac{P(1 - \epsilon_i)}{B_0 B_{q_c}^2} \right) \rho_v^{02} \bar{\tau} + O\left(\frac{1}{A_0}\right) \simeq \frac{\epsilon_v P b_c \bar{\tau}}{\rho_v^0} + O\left(\frac{1}{A_0^2}\right), \quad (46)$$

$$\xi_0^2 = \frac{\sqrt{1 + B}(B - \bar{\epsilon})^2}{8B^3}. \quad (47)$$

Furthermore, in this approximation ($\tau_C \gg \tau_I \gg \tau_V$), interstitial loop and void densities may be expressed as linear combinations of the eigenmodes of the linear evolution matrix, and this leads to the following relations which express how they are linked to the vacancy loop density:

$$\delta \rho_{Iq_c} \simeq -\frac{\epsilon_v}{\rho_v^0 \epsilon_i} \delta \rho_{Vq_c}, \quad (48)$$

$$\delta \rho_{Cq_c} \simeq \frac{(B + \bar{\epsilon})}{B(1 + B)} \frac{\rho_v^0}{1 + \rho_i^0 + \rho_v^0} \delta \rho_{Vq_c}. \quad (49)$$

It is interesting to recall here that ρ_v^0 increases with dose while $\rho_v^0/(1 + \rho_i^0 + \rho_v^0)$ tends to a constant. As a result, the amplitudes of the inhomogeneities in the interstitial loop distribution decrease with dose, contrary to the amplitude of the inhomogeneities in the void density which are proportional to the amplitude of the vacancy loop microstructure.

Equation (42) has the generic structure of order-parameter equations describing reaction-diffusion systems close to a Turing instability. It is known to give rise to stripe or hexagonal structures in two-dimensional systems, and to BCC lattices, hexagonal prisms or planar wall structures in three-dimensional systems. Hexagonal and BCC structures appear sub critically, via an inverted bifurcation, while stripes or walls appear super critically, via a supercritical bifurcation. The width of the subcritical region decreases with irradiation dose [64, 133]. The expected sequence of selected patterns that should develop for increasing time or irradiation dose is thus: BCC lattices at low irradiation dose and planar arrays at high irradiation dose [62].

5.5. ANISOTROPY EFFECTS

The analysis described in the preceding sections is isotropic, and does not take into account anisotropies related to the crystal structure. However, crystal lattice effects on nano- and microstructure selection is an important issue, especially for the formation of void lattices that are isomorphic with their host crystal lattice, as most experimental observations show. A partial answer to this problem has been obtained by taking into account the anisotropy of interstitial atom diffusion. MD simulations suggest that Self-Interstitial Atoms (SIAs) and glissile interstitial clusters migrate preferentially along closely-packed crystallographic directions. In this case, we showed [61] that the dislocation microstructure should be oriented parallel to the directions of high interstitial cluster mobility. Hence, at low irradiation dose, the loop and void structures should exist in parallel orientations to the underlying crystal lattice with the same symmetry, while at high irradiation dose, they consist of planar arrays. These arrays should nevertheless have their planes parallel to closely packed crystalline axes.

5.6. NUMERICAL ANALYSIS

In principle, the results of the weakly nonlinear analysis described above are only valid close to the instability threshold. Hence, this analysis could become irrelevant for long irradiation times or high irradiation dose, when these approximations are supposed to break down. Under such conditions, the numerical analysis of the complete dynamical model remains the only way to test the validity of the weakly nonlinear analysis and to follow the complete evolution of the nano- and microstructure.

The numerical integration of the evolution equations of defect densities has been performed in one and two spatial dimensions using an implicit Euler method [63]. The four variable fields (point defects and loop densities) have initialized on uniform states. Then an initial 1% noise has been added to point defect densities. Since point defect densities evolve much more rapidly (by several orders of magnitude) than the loop densities, their evolution equations were solved implicitly, while the loop evolution equations were solved explicitly.

The following main results have been obtained [63]:

Wavelength selection in one dimension

In one spatial dimension, for a numerical system consisting of 512 elementary cells, and with no-flux boundary conditions, the integration has been performed for several typical irradiation and material conditions at different temperatures (low temperature: $T = 500^\circ$ or high temperature: $T = 700^\circ$), irradiation dose (accelerator conditions: $P = 10^{-3}$ dpa s^{-1} or reactor conditions: $P = 10^{-6}$ dpa s^{-1}), and network dislocation density (cold-worked nickel: $\rho_N = 10^{15}$ m^{-2} or annealed nickel: $\rho_N = 10^{13}$ m^{-2}). For this wide range of investigated conditions, the numerical simulations confirm the results of the linear stability analysis. The results are summarized in Table 4 where stability, critical dose and critical wavelength are presented. The parameters used for the numerical analysis are listed in Table 5.

Furthermore, nano- and microstructure evolution in one-dimensional systems may be summarized as follows [63]. During early irradiation times, linear terms are responsible for wavelength selection. Selected modes rapidly grow. As time proceeds, the eigenvalues associated with stable modes go to zero. This effect, combined with the presence of nonlinear terms, triggers the generation of initial unstable mode harmonics. These are responsible for sharpening of the loop density profile, or, in other words, for the accumulation of defects in very localized, though regularly spaced regions.

Table 4. Numerical results for one-dimensional systems

ρ_N (m^{-2})	P (dpa s^{-1})	instability	critical dose (dpa)	q_c (m^{-1})	selected λ (nm)
10^{13}	10^{-3}	Yes	0.025	1.3×10^7	170
10^{13}	10^{-6}	Yes	0.03	1.4×10^7	160
10^{15}	10^{-3}	Yes	$\simeq 0$ dpa	5.4×10^7	100
10^{15}	10^{-6}	No	–	–	–

Table 5. Material parameters for nickel

Parameter	Symbol	Value	Units
Vacancy diffusion	D_v	$6 \times 10^{-5} e^{-1.3 \text{ eV}/k_B T}$	$\text{m}^2 \text{ s}^{-1}$
Interstitial diffusion	D_i	$10^{-7} e^{-0.3 \text{ eV}/k_B T}$	$\text{m}^2 \text{ s}^{-1}$
Equilibrium vacancy concentration	c_v^e	$e^{-1.6 \text{ eV}/k_B T}$	–
Stacking fault energy	γ_{sf}	9.4×10^{16}	eV m^{-2}
Shear modulus	$\mu/(1 - \nu)$	8×10^{10}	Pa m^{-2}
Burgers vector	b	2.5×10^{-10}	m
Atomic volume	Ω	1.206×10^{-29}	m^3
Network bias excess	B	0.1	–
Loop/network bias excess	ΔB	0.05	–
Initial vacancy loop radius	r_v^0	1.5×10^{-9}	m
Network dislocation density	ρ_n	$10^{13} - 10^{15}$	m^{-2}
Displacement damage rate	P	$10^{-6} - 10^{-3}$	dpa^{-1}
Cascade collapse efficiency	ϵ_v	0.01 – 0.1	–
Interstitial loop density	N	$10^{20} - 10^{22}$	m^{-3}
Temperature	T	773 – 973	P

Pattern selection and anisotropy effects in two dimensions

The results of numerical analysis performed in [63] on (128×128) grids with periodic boundary conditions presents the same characteristics as for one-dimensional systems, as far as the wavelength and the coarsening of the loop distributions are concerned. With respect to the symmetry of the structures, the weakly nonlinear analysis predicts a final wall (3D) or striped (2D) structure. On the other hand, and in other extended pattern forming systems, striped structures usually present a lack of orientational order, due to the presence of topological defects. It is only in anisotropic systems that regular parallel rolls or stripes may be observed [64].

This behavior is also observed here, as illustrated in Fig. 8. For isotropic point defect diffusion, the structure evolves towards mosaic-like patterns, with no well defined orientation for the high loop concentration bands. The final structure resembles more regularly spaced defect clusters. However, in the case of anisotropic interstitial diffusion, well defined bands are obtained, in parallel orientation with high interstitial cluster mobility directions. We see thus here the confirmation that the anisotropies triggered by the crystalline structure of the

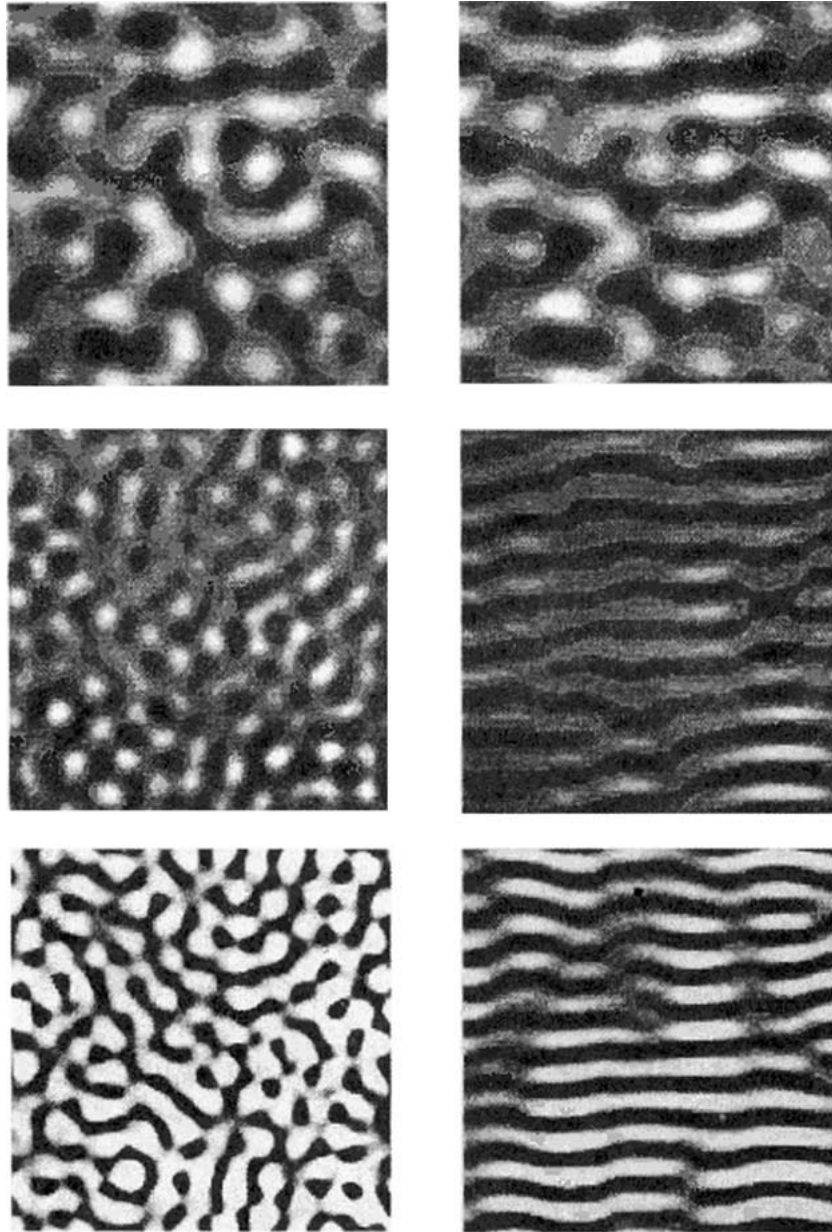


Figure 8. Snapshots of the two-dimensional evolution of the amplitude of the vacancy loops microstructure ($\delta\rho_V$) in space at different irradiation doses for annealed nickel under typical accelerator conditions and low temperatures ($\rho_N = 10^{13} \text{ m}^{-2}$, $P = 10^{-3} \text{ dpa s}^{-1}$, $T = 773 \text{ K}$) in the case of isotropic point defect diffusion (left column)(the dose is increasing from 1 dpa in the upper graph to 20 dpa in the lower graph), and with a 1% anisotropy in the interstitials diffusion coefficient (right column) (the dose is increasing from 1 dpa in the upper graph to 20 dpa in the lower graph).

material are essential in determination of the orientation of the nano- and microstructure, as observed in experiments [32, 65]. This should also be true for void lattice according to our model, since their spatial organization originates in loop instability.

From this observation, and the weakly nonlinear analysis showing that the most unstable wave vectors are perpendicular to the high mobility directions of the interstitials, one may thus infer the following scenarios for three-dimensional self-organization of loops. If the interstitial mobility is maximum for one set of planes, the defect nano- and microstructure should evolve towards regularly spaced walls parallel to these planes. If the interstitial mobility is maximum for two sets of planes, the defect nano- and microstructure should evolve towards a labyrinth structure formed of domains of walls parallel to one or the other set of high mobility planes (cellular or bimodal structures are effectively ruled out by scalar nonlinearities [64]). If the interstitial mobility is maximum in one direction, say z , the most unstable wave vectors will be isotropically distributed in the plane perpendicular to the easy axis, say the (x, y) plane. Hence, the resulting loop distribution should not vary in the z direction, but well in the (x, y) planes where it should present the same microstructure as the ones obtained in two-dimensional isotropic systems and presented in Fig. 8.

6. Comparison between theory and experiment

The group of models described in this article contain space-time rate equations for mobile point defects (vacancies and self-interstitials), with anisotropic diffusion for only the interstitial population. They also contain coupled space-independent rate equations for the densities of dislocation loops (represented by vacancy and interstitial loops), as well as voids. The onset of spatial instabilities is analyzed through the linear part of evolution equations. Even when voids are present at high temperature, spatial instabilities are driven by perturbations in the vacancy cluster (loop) density. From the previous models, it is concluded that two general conditions must be satisfied for the formation of patterned nano- and microstructure in irradiated materials:

1. The rate of point defect absorption on the initial microstructure (first order reaction) must dominate over their mutual recombination (second-order reaction). This is satisfied by Eq. (12).
2. Cascade-induced vacancy cluster densities must reach a critical value. This critical concentration is determined by the initial microstructure (i.e., annealed versus cold-worked), the dislocation bias, and the cascade collapse efficiency. This condition is satisfied by Eq. (36).

We will first discuss the general qualitative agreements between the rate theory predictions and experimental observations, and then turn our attention to areas of quantitative agreements and un-resolved discrepancies.

Numerical simulations verify the analytical conclusions, and show that spatially organized defect microstructure is difficult to obtain for an initially cold-worked material. Direct numerical simulations of the kinetic model introduced in [63] have largely confirmed the qualitative conclusions drawn on the basis of the weakly nonlinear analysis. However, the wavelength of emerging patterns is shown to be somewhat insensitive to the irradiation dose. These two aspects are in general qualitative agreement with experimental observations. Numerical simulations have been performed for both cold-worked and annealed nickel under typical accelerator ($P = 10^{-3}$ dpa s^{-1}) and reactor ($P = 10^{-6}$ dpa s^{-1}) conditions. It is shown

that during early irradiation times, linear terms controlled by the the critical vacancy cluster density, the cascade collapse efficiency and the dislocation bias, are responsible for wavelength selection. As time proceeds, eigenmodes associated with stable components decay, while nonlinear terms trigger higher harmonic generation of unstable modes. The final effect is a rapid sharpening of the concentration of immobile defects into walls, with very few left in-between. These theoretical predictions of the evolution sequence are also consistent with the experimental observations that the nano- and micro-structure patterns are built up gradually, and that they first start from poorly aligned spatial inhomogeneities, and finally sharpen to well-defined super-lattices.

Weakly non-linear analysis of the isotropic model predicts a final wall (in 3-D) or striped (in 2-D) defect structures. Numerical simulations verify these conclusions in two-dimensional systems, where striped defect wall arrangements, with no preferred direction, are obtained when interstitial diffusion is assumed to be isotropic. On the other hand, only 1% anisotropy in the diffusion coefficient of self-interstitials along a preferred direction (i.e. $\langle 110 \rangle$), is shown to result in significant alignment of clustered defects in $\langle 110 \rangle$ -directions (or on $\{100\}$ -planes), in agreement with numerous experimental observations on Ni, and with Jäger's experimental observations on Cu. While the diffusional anisotropy of SIAs is not a necessary pre-requisite for the onset of the spatial instability, it appears to be necessary for the isomorphism of the micro-structure superlattice with the underlying crystal structure. Only a small degree of interstitial atom diffusional anisotropy is needed to result in significant alignment of clustered defects along $\langle 110 \rangle$ -directions, because unstable wave vectors are preferred along highly-packed crystal directions. This effect influences void distributions in a similar way, since it has been shown in our model that spatial fluctuations of the void density is directly related to spatial fluctuations of the vacancy cluster density. In the absence of any diffusional anisotropy, the theory predicts that the microstructure should evolve from a random, spatially uniform distribution to a BCC structure and finally to striped or wall structures. However, experimental observations indicate that the microstructure pattern is always tied up with the host crystal lattice. In the case of void and bubble lattices, the selected pattern is isomorphic with the crystal lattice, while in the case of vacancy clusters, the alignment is also crystallographic, but tends to result in one-dimensional walls or striped zig-zag structures. The explanation of this particular feature relies on including anisotropies in the theory (interaction or diffusional), but the degree of deviation from isotropic behavior needs not be very large. As shown in the theory, only 1% diffusional anisotropy in SIA transport was found to be sufficient to trigger fast growing wave vector perturbations along crystallographic directions. These compete with other modes, but dominate the dynamics at the end.

Aspects of quantitative agreement between theory and experiment rely on the level of detail available to us from experimental measurements. Two types of observations are clearly established by experimental methods. These are: (1) The *phase boundaries* between aligned and random microstructure, as represented in Figs. 1 and 2. It is clear that for the case of irradiated Ni, two phase boundaries (in the P-T phase space) exist, where aligned microstructure is experimentally observed. (2) The magnitude of the *wavelength* for self-organized microstructure, as can be ascertained from Tables 1–3.

The experimental data for irradiated Ni is re-plotted in Fig. 9 in the form of a *phase diagram*, where approximate phase boundaries between uniform and ordered microstructure are also shown. The abscissa represents $x = T_m/T$, while the ordinate stands for $y = \log P$. The recombination dominance condition of Eq. (12), when the material constants of Ni irradiation (cf., Table 5) are used, can be approximately re-written as:

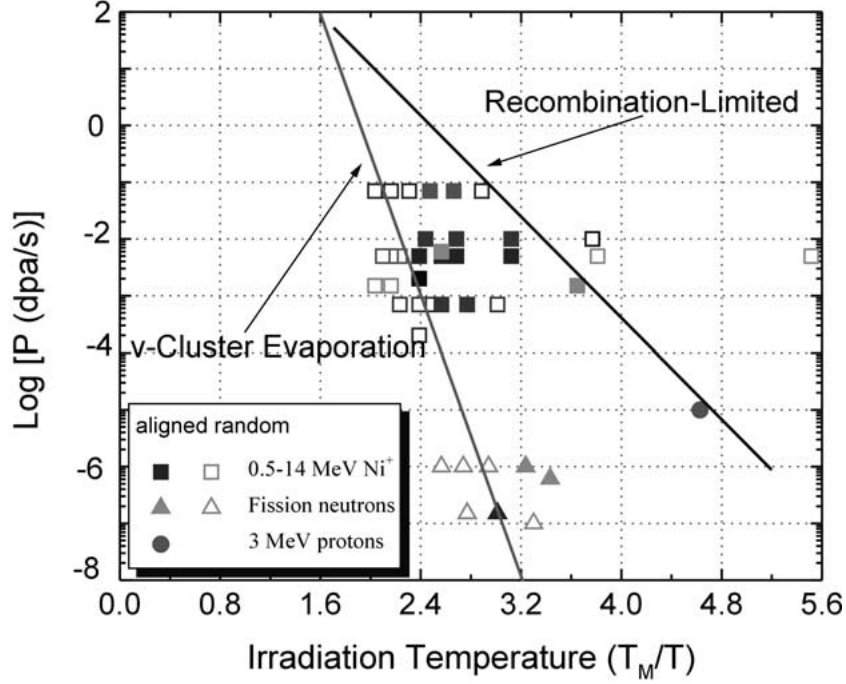


Figure 9. Comparison between experimental data and theoretical predictions for the temperature and dose rate dependence of defect cluster wall observations in irradiated nickel. The data include Ni+ ion [66–68, 70], fission neutron [28, 74], and proton [65, 72] irradiations. The filled symbols denote conditions where defect cluster wall formation was observed.

$$P \simeq \left(\frac{\rho_N a^2 \omega}{4S} \right) e^{-E_v^m/kT} \simeq 1.25 \times 10^4 e^{-E_v^m/kT}, \quad (50)$$

where we used an average value for the initial sink (dislocation) density of $\rho_N = 2 \times 10^{14} \text{ m}^{-2}$ as the only adjustable parameter in the equation, while the lattice constant $a = 0.36 \text{ nm}$, the vibrational frequency $\omega = 5 \times 10^{13} \text{ Hz}$, and the recombination combinatorial number $S = 10$ are standard values. In the phase space represented in Fig. 9, the previous equation is a simple straight line: $y = mx + b$, where the intercept $b \simeq 4.1$, and the slope $m = (-E_v^m/kT_m) \log e$. This simple procedure results in a vacancy migration energy $E_v^m \simeq 1 \text{ eV}$, compared to an experimental value of 1.2–1.3 eV, and the theoretical intercept of 4.1 corresponds to a value of $\simeq 5$ obtained from extending the phase boundary line to the origin in Fig. 9. The results of this approximate analysis (i.e., vacancy migration energy, average initial sink density, and linear relationship between $\log P$ and T_m/T) are all in good agreement with the experimental data, as can be seen in Fig. 9.

The high temperature phase boundary is determined when the bifurcation parameter (i.e., ratio of vacancy cluster sink density to the total sink density) exceeds a critical value governed by the production and absorption asymmetries (biases) for the disposition of point defects. It is mainly dictated by stage V activation energy (E_v^B) rather than its migration energy, because the thermal stability of vacancy clusters is controlled by the magnitude E_v^B . The steepness of the high-temperature boundary compared to its low-temperature part is consistent with the experimental fact that $E_v^B > E_v^m$. However, the exact location of this boundary is governed by several processes (e.g., initial sink density, production bias, absorption bias), and thus must

be computed numerically. This condition has been numerically evaluated in reference [62], and the results are in reasonable agreement with the boundary of Fig. 9. However, it must be noted that this boundary can be totally eliminated if, for example, the initial sink structure is very high suppressing the formation of destabilizing vacancy clusters (as in cold-worked materials), or the inherent characteristics of the cascade collapse mechanism is such that a small percentage of vacancy clusters are produced.

This last point leads us to the apparent difficulties in formation of organized nano- and micro-structures in irradiated copper, as well as in alloys and BCC metals, as discussed earlier in Section 3. From geometric considerations, preferential one-dimensional migration of small interstitial clusters along $\langle 110 \rangle$ -directions would lead to the formation of $\{001\}$ -walls of vacancy clusters [99]. This potential mechanism for defect cluster patterning suggests that the resistance of copper to form defect cluster walls under energetic displacement cascade conditions could be due to the lack of one-dimensional migration of interstitial clusters, perhaps due to preferential formation of large (sessile) interstitial clusters during the thermal spike phase for high PKA energy irradiation (e.g., fission neutrons and self-ions). The decreased production ratio of sessile (as compared to glissile) defect clusters in copper irradiated at lower average PKA energies (e.g., 3-MeV protons) could promote wall formation. However, this does not explain the absence of defect cluster patterning in copper irradiated with 0.4 MeV H or 0.8 MeV He ions [100]. It is worth pointing out that the production of a large number of sessile vacancy and interstitial clusters in copper under energetic displacement cascade conditions leads to a rapid buildup of sink density. Consequently, fewer glissile interstitial clusters are likely to escape to participate in the process of aligned pattern formation. This high sink density mechanism may be an additional reason for the lack of pattern formation in copper under energetic displacement cascade conditions. In the case of nickel, on the other hand, the relatively high fraction of mobile defects and low fraction of sessile defect clusters (Fig. 4) produced in energetic displacement cascades should result in conditions favorable for defect cluster patterning. Since clearly aligned defect patterns have only been observed by Jäger and coworkers [32, 72], the agreement between theory and experiment is not totally satisfactory, suggesting that additional experiments aimed at clarifying this discrepancy are needed.

Experimental observations for the selected wavelength (superlattice spacing) of gas bubbles (Table 3) show that the wavelength is rather small, and that its range is also limited (i.e., 5–12 nm). However, the superlattice spacing observed in many experiments on void formation (Table 2) is larger, and shows a considerable spread in values (i.e., 22–145 nm). Results of numerical calculations for approximate one-dimensional systems (Table 4) show that the theoretical wavelength is in the range of 100–170 nm. Predicted wavelength values given by Eq. (37) are larger still, and signify the initiation of an instability via the critical wave vector. Numerical simulations show, however, that the discrepancy between the critical wavenumber (q_c), and the one that is finally selected can be explained by the dominance of the third harmonic ($3q_c$) as a result of non-linear interactions when the irradiation dose increases. Based on numerical analysis of the system's non-linear dynamics, the experimental values for void superlattices are somewhat smaller than those predicted by computer simulations. However, the values computed by Eq. (37), which is derived from linear stability analysis, are about 3 times larger than experiment. A qualitative argument for this difference between linear and non-linear results can be made as follows. Both the $2q_c$ and $3q_c$ modes are generated by critical ones, but the amplitude of $3q_c$ modes is proportional to $\sqrt{\rho_v}$, which increases with dose, while the $2q_c$ does not. Thus, the content of $3q_c$ mode should increase with irradiation

dose, and may explain the larger wavelength predicted by the theory as compared to experimental observations. The smaller wavelength for bubble superlattice formation is not entirely explained by the present models, and may be a result of the higher nucleation rates of bubbles as opposed to voids.

7. Summary and conclusions

One may conclude that a comprehensive theoretical framework for the analysis of spatial instabilities in the nano- and microstructure of irradiated materials has now been obtained. This framework, which was initiated over two decades ago, results from the succession of works based on a well-established rate theory of microstructure evolution under irradiation. The theory has been pursued both qualitatively and numerically to ascertain the main processes leading to nano-structure pattern selection in irradiated materials. Throughout this review, we emphasized theoretical conditions, which are consistent with experimental observations, for the development of spatially organized (or self-assembled) nano-structures. Some areas which still lack clear understanding include the effects of void density on the magnitude of the selected wavelength, the smaller wavelength of bubble lattices as compared to void lattices, and the unique conditions that lead to loop patterning in Cu.

The rate theory kinetic models described here incorporate basic elements of defect generation, interactions and mobility. They also allow an explicit determination of the instability threshold and its dependence on material and irradiation parameters. Determination of selected nano-structure and its subsequent evolution requires post-bifurcation analysis. Such analysis may be performed analytically and numerically [63]. In the weakly non-linear regime, the analysis is based on a derivation of density perturbations for the Fourier components of immobile defects, by invoking a quasi-static approximation. With this approximation, Ginzburg–Landau type amplitude equations for the nano-structure may be derived, with slowly varying time-(or dose-)dependent coefficients. Generic conclusions of pattern selection theory are then recovered, showing non equilibrium phase transitions leading to the eventual formation of wall defect structures, with a wavelength that decreases with the irradiation dose. Furthermore, the nano-structure is expected to be extremely sensitive to even small anisotropies. In particular it should have parallel orientations with the directions of high interstitial mobility, as is experimentally observed for vacancy cluster walls, and for void and bubble super-lattices as well.

The results of the theory are in general agreement with the majority of experimental observations. Most of the qualitative features of self-assembled nano-structures can be explained on the basis of the present level of theoretical development. Theory predictions for the gradual transition from spatially random to self-assembled nano-structure, the insensitivity of the selected wavelength to temperature and its weak dependence on dose rate, the isomorphism between the nano-structure super-lattice and the underlying crystal, the decrease of observed wavelength with dose and the zig-zag patterns of vacancy clusters are all in qualitative agreement with experimental observations. Surprisingly good quantitative agreement between theory and experiment is obtained for the phase boundaries between ordered and random nano-structures, and for the magnitude of the selected pattern wavelength. On the other hand, the apparent experimental difficulty in verifying the exact mechanism responsible for pattern formation in irradiated copper is somewhat unresolved. While Jäger clearly showed well-defined self-assembled vacancy clusters in copper, the majority of other experimental

results did not show pattern formation. To resolve the fundamental differences that lead to such unusual on/off condition within the framework of the current theory require additional specifically planned experiments.

In summary, the necessary ingredients for the kinetic rate theory model to be consistent with experimental observations are three. These are:

1. An excess bias of dislocations towards interstitial atom absorption.
2. A fraction of vacancies to be produced directly in clusters, as a result of collision cascades.
3. A small degree of interstitial diffusional anisotropy.

The production asymmetry (so called production bias) appears not to be essential to triggering microstructure instabilities (i.e., $\varepsilon_i = 0$), as long as a small fraction of vacancies is produced in clustered sessile configurations. However, if sessile SIA clusters are also produced in collision cascades (i.e., $\varepsilon_i \neq 0$), their presence combines to accelerate the onset of spatial instabilities.

Acknowledgements

This work is supported by the US Department of Energy, Office of Fusion Energy Sciences, Grant DE-FG03-98ER54500 with UCLA, and contract DE-AC05-00OR22725 with UT-Battelle, LLC (ORNL). Financial assistance through a grant from the Belgian National Fund for Scientific Research is gratefully acknowledged. The authors benefited from numerous discussions throughout the course of this work with the following: C. Abromeit, J. H. Evans, W. Jäger, G. Martin, S. Murphy, A. Semenov, B. N. Singh, H. Trinkaus, and C. Woo. This article is dedicated to the memory of K. Krishan, whose contributions stimulated much of the interest in applying dynamical system theory to the understanding of self-organization in irradiated materials.

References

1. Nicolis, G., Dewel, G. and Turner, J. (Eds.), *Order and Fluctuations in Equilibrium and Nonequilibrium Statistical Mechanics*, Wiley Publishers, New York, 1981.
2. Walgraef, D., *Spatio-Temporal Pattern Formation with Examples in Physics, Chemistry and Materials Science*, Springer-Verlag, New York, 1996.
3. Busse, F. and Kramer, L. (Eds.), *Nonlinear Evolution of Spatio-Temporal Structures in Dissipative Continuous Systems*, Plenum Press, New York, 1990.
4. Cross, M.C. and Hohenberg, P.C, *Rev. Mod. Phys.*, 65, (1993) 851.
5. Borckmans P., Dewel G., De Wit A., and Walgraef D., Turing bifurcations and pattern selection, in *Chemical Waves and Patterns*, Kapral R., and Showalter K. (Eds.), Kluwer, Dordrecht, pp. 323–363 (1994).
6. Baras, F. and Walgraef, D., *Physica, A* 188 (1992).
7. Bodenschatz, E., Zimmermann, W. and Kramer, L., *J.Phys.*, 49 (1988) 875.
8. Rehberg, I., Winkler, B.L., de la Torre Juarez, M., Rasenat, S. and Schopf, W., *Festkörperprobleme/Advances in Solid State Physics*, 29 (1989) 35.
9. Busse, F.H., *Rep. Prog. Phys.*, 41 (1978) 1929.
10. Busse, F.H. and Riahi, N., *J. Fluid Mech.*, 96 (1980) 243.
11. Sivashinsky, G.I., *Physica, D* 8 (1983) 243.
12. López-Salvans, M.Q., Sagués, F. and Claret, J., Fingering in Thin Layer Electrodeposition, in: the Proceedings of the 1st Latin American School on Materials Instabilities, held in Valparaiso, Chile, Dec 98, Kluwer Publication, 2000.
13. Neuhauser, H., Plastic Instabilities and the Deformation of Metals, in: *Patterns, Defects and Materials Instabilities*, Walgraef, D. and Ghoniem, N.M. (Eds.), Kluwer Academic Publishers, Dordrecht, 1990.
14. Kratochvil, J., *Rev. Phys. Appliquée*, 23 (1988) 419.

15. Kossowsky, R., Singhal, S.C., *Surface Engineering, Surface Modification of Materials*, Martinus Nijhoff, Dordrecht, 1984.
16. Bauerle D., *Laser Processing and Chemistry*, Springer-Verlag, New York, 1996.
17. Evans, J.H., *Nature*, 29 (1971) 403; *Rad., Eff.* 10 (1971) 55.
18. Seul, M. and Wolfe, R., *Phys. Rev. A*, 46 (1992) 7534.
19. Roco M.C., Williams S. and Alivisatos P. (Eds.), 'Nanotechnology Research Directions: IWGN Workshop Report Vision for Nanotechnology Research and Development in the Next Decade', WTEC, Loyola College in Maryland, September 1999.
20. Suo, Z. and Lu, W., 'Self-Organizing Nanophases on a Solid Surface', prepared for a book dedicated to Professor James R Rice on the occasion of his 60th birthday, edited by T.J. Chuang (Ed.), to be published by Kluwer Academic Publishers, Dordrecht, in press.
21. Lu, W. and Suo, Z., Dynamics of nanoscale pattern formation of an epitaxial monolayer, prepared for a special issue of *Journal of the Mechanics and Physics of Solids* dedicated to Professors of J.W. Hutchinson and J.R. Rice on the occasion of their 60 th birthdays.
22. Suo, Z. and Lu, W., 'Forces that Drive Self-Assembly on Solid Surfaces', accepted by *J. Nanoparticles Res.*, October 2000.
23. Sass, S. and Eyre, B.L., *Philos. Mag.*, 27 (1973) 1447.
24. Johnson, P.B., Mazey, D.J. and Evans J.H., *Radiat. Eff.*, 78 (1983) 147.
25. Mazey, D.J. and Evans, J.H., *J. Nucl. Mater.*, 138 (1986) 16.
26. Evans, J.H. and Mazey, D.J., *J. Phys.*, F15, L1 (1985); Evans, J.H., *J. Nucl. Mat.*, 132 (1985) 147.; *J. Nucl. Mat.*, 138 (1986) 176.
27. Jostons, A. and Farrell, K., *Radiat. Eff.*, 15 (1972) 217.
28. Stiegler, J.O. and Farrell, K., *Scr. Metall.*, 8 (1974) 651.
29. Kulcinski, G.L., Brimhall, J.L. and Kissinger, H.E., in: *Proceedings of the International Conference on Radiation-Induced Voids in Metals*, Albany, NY, June 1971, CONF-710601, Corbett, J.W. and Iannello, L.C. (Eds.), National Technical Information Service, Springfield, VA, 1972, p. 465.
30. Wiffen, F.W., in: *Proceedings of the International Conference on Radiation-Induced Voids in Metals*, Albany, NY, June 1971, CONF-710601, Corbett, J.W. and Iannello, L.C. (Eds.), National Technical Information Service, Springfield, VA, 1972, p. 386.
31. Singh, B.N. and Evans, J.H., *J. Nucl. Mat.*, 226, (1995) 277.
32. Jäger, W. and Trinkaus, H., *J. Nucl. Mater.*, 205 (1993) 394 .
33. Amodeo, R.J. and Ghoniem, N.M., *Res Mechanica*, 23 (1988) 137.
34. Evans, J.H. in *Patterns, Defects and Materials Instabilities*, Walgraef D. and Ghoniem N.M. (Eds.), Kluwer Academic Publisher, Dordrecht, 1990, pp. 347–370.
35. Malen, K. and Bullough R. in *Proc. Int. Conf. on Voids Formed by Irradiation of Reactor Materials*, Reading, UK, 1970, Brit. Nucl. Energy Society, p. 109.
36. Johnson, E. and Chadderton, L.T., *Rad. Effects*, 79 (1983) 183.
37. Khachatryan, A.G. and Airapatyan, V.M., *Phys. Stat. Solidii*, A26 (1974) 61.
38. Foreman, A.J.E., *AERE Reports*, No. 7135, Harwell, England, (1972).
39. Woo, C.H. and Frank, W., *J. Nucl. Mater.*, 137 (1985) 7, 140 (1986) 214, 148 (1987) 121, *J. Nucl. Mater.*, 206 (1993) 170.
40. Frank, W. in *Nonlinear Phenomena in Materials Science*, Aussois 1987, Kubin L.P. and Martin G. (Eds.), *Trans. Tech.*, Aedermannsdorf, Switzerland, 1988, p. 315.
41. Evans, J.H., *J. Nucl. Mat.*, 119 (1983) 180.
42. Evans, J.H. in *Nonlinear Phenomena in Materials Science*, Aussois 1987, Kubin L.P. and Martin G. (Eds.), *Trans Tech*, Aedermannsdorf, Switzerland, 1988, p. 303.
43. Dubinko, V.I., Tur A.V., Turkin, A.A. and Yanovsky V.V., *J. Nucl. Mater.*, 161 (1989) 57.
44. Diaz de la Rubia, T., Averbach, R.S., Hsieh, H. and Benedek, R., *J. Mater. Res.*, 4 (1989) 579.
45. Diaz de la Rubia, T., Averbach, R.S., Benedek, R. and Robertson, I.M., *Rad. Eff. Def. Solids*, 113 (1990) 39.
46. Finnis, M.W., Agnew, P. and Foreman, A.J.E., *Phys. Rev.*, B44 (1991) 567.
47. Foreman, A.J.E., English, C.A. and Phythian, W.J., *Phil. Mag.*, A66 (1992) 655.
48. Phythian, W.J., Stoller, R.E., Foreman, A.J.E., Calder, A.F. and Bacon, D.J., *J. Nucl. Mater.*, 223 (1995) 245.
49. Zinkle, S.J. and Singh, B.N., *J. Nucl. Mater.*, 199 (1993) 173.

50. Woo, C.H., Semenov, A.A. and Singh, B.N., *J. Nucl. Mater.*, 206 (1993) 170.
51. Krishan, K., *Nature*, 287 (1980) 420.
52. Foreman, A.J.E. and Makin, M.J., *J. Nucl. Mater.*, 79 (1979) 43.
53. Krishan, K., *Radiat. Eff.*, 66 (1982) 121.
54. Krishan, K., *Phil. Mag.*, A45 (1982) 401.
55. Muncie, J.W., Eyre, B.L. and English, C.A., *Phil. Mag.*, A52 (1985) 309.
56. Murphy, S.M., *Europhys. Lett.*, 3 (1987) 1267.
57. Abromeit, C. and Martin, G., *Solid State Phenomena*, 3-4 (1988) 321.
58. Koptelov, E.A. and Semenov, A.A., *J. Nucl. Mater.*, 160 (1988) 253.
59. Krishan, K., *Solid State Phenomena*, 3-4 (1988) 267.
60. Abromeit, C., *Intern. J. Mod. Phys.*, B3 (1989) 1301.
61. Walgraef, D. and Ghoniem, N.M., *Phys. Rev.*, B39 (1989) 8867.
62. Ghoniem, N.M. and Walgraef, D., *Model. Simul. Mater. Sci. Eng.*, 1 (1993) 569.
63. Walgraef, D., Lauzeral, J. and Ghoniem, N.M., *Phys. Rev.*, B53 (1996) 14782.
64. Walgraef, D., *Spatio-Temporal Pattern Formation*, Springer-Verlag, New York, 1996.
65. Jäger, W., Ehrhart, P. and Schilling, W., *Solid State Phenomena*, 3-4 (1988) 297; *Radiat. Eff. Def. Solids*, 113 (1990) 201.
66. Kulcinski, G.L. and Brimhall J.L., in: *Effects of radiation on substructure and mechanical properties of metals and alloys*, Motteff J. ed., ASTM STP 529, American Society for Testing and Materials, Philadelphia, 1973, p. 258.
67. Brimhall, J.L., Battelle Pacific Northwest Laboratory report BNWL-1839 (1974).
68. Westmoreland, J.E., Sprague J.A., Smidt F.A. and Malmberg P.R., *Rad. Eff.*, 26 (1975) 1.
69. Regnier, P. and Glowinski, L.D., *J. Nucl. Mater.*, 57 (1975) 243.
70. Whitley, J.B., Ph.D Thesis, Nuclear Engineering Department, University of Wisconsin, (1978).
71. Bullen, D.B., Ph.D. Thesis, Nuclear Engineering Department, University of Wisconsin, 1984.
72. Jäger W., Ehrhart P., Schilling W., Dworschak F., Gadalla A.A. and Tsukuda N., *Mater. Sci. Forum*, 15-18 (1987) 881.
73. Martin, G., Bocquet, J.L., Barbu A., Adda A., in: *Radiation Effects in Breeder Reactor Structural Materials*, Bleiberg, M.I., and Bennett, J.W. (Eds.), TMS-AIME Publication, New York, 1977, p. 899.
74. Zinkle, S.J. and Snead, L.L., *J. Nucl. Mater.*, 225 (1995) 132.
75. Stathopoulos, A.Y., *Phil. Mag.*, A44 (1981) 285; also Stathopoulos A.Y., English, C.A., Eyre, B.L. and Hirsch, P.B., *ibid.* 309.
76. Kirk, M.A., Robertson, I.M., Jenkins, M.L., English, C.A., Black, T.J. and Vetrano, J.S., *J. Nucl. Mater.*, 149 (1987) 21.
77. Vetrano, J.S., Robertson, I.M. and Kirk, M.A., *Scripta Met.*, 24 (1990) 157.
78. English, C.A., *Rad. Eff. Def. Solids*, 113 (1990) 15.
79. Robertson, I.M., Vetrano, J.S., Kirk, M.A. and Jenkins, M.L., *Phil. Mag.*, A63 (1991) 299.
80. Jenkins, M.L., Kirk, M.A. and Phythian, W.J., *J. Nucl. Mater.*, 205 (1993) 16.
81. Robertson, I.M., Tappin, D.K. and Kirk, M.A., *Phil. Mag.*, A68 (1993) 843.
82. Kim, S-J, Nicolet, M-A, Averbach, R.S. and Peak, D., *Phys. Rev.*, B37 (1988) 38.
83. Jung, P., *Phys. Rev.*, B23 (1981) 664.
84. Klabunde, C.E. and Coltman, R.R. Jr., *J. Nucl. Mater.*, 108&109 (1982) 183.
85. Guinan, M.W., Kinney, J.H. and Van Konynenburg, R.A., *J. Nucl. Mater.*, 133-134 (1985) 357.
86. Wallner, G., Anand, M.S., Greenwood, L.R., Kirk M.A., Mansel W. and Waschkowski W., *J. Nucl. Mater.*, 152 (1988) 146.
87. Singh, B.N., Horsewell, A., Toft, P. and Edwards, D.J., *J. Nucl. Mater.*, 224 (1995) 131.
88. Zinkle, S.J., Kulcinski, G.L. and Knoll, R.W., *J. Nucl. Mater.*, 138 (1986) 46.
89. Zinkle, S.J. and Farrell, K., *J. Nucl. Mater.*, 168 (1989) 262.
90. Zinkle, S.J., Snead, L.L., Singh, B.N., Edwards D.J., in: *Fusion Materials Semiannual Progress Report*, 1994, DOE/ER-0313/17, Oak Ridge National Lab, (1994), p. 69.
91. Zinkle, S.J., Horsewell, A., Singh, B.N. and Sommer, W.F., *J. Nucl. Mater.*, 212-215 (1994) 132.
92. Wolfenden, A., *Rad. Effects*, 15 (1972) 255.
93. Muroga, T., Yoshida, N., Tsukuda, N., Kitajima, K. and Eguchi, M., *Mat. Sci. Forum*, 15-18 (1987) 1087.
94. Horsewell, A., Singh, B.N., Proennecke, S., Sommer, W.F. and Heinisch, H.L., *J. Nucl. Mater.*, 179-181 (1991) 924.

95. Yoshida, N. and Kiritani, M., *J. Phys. Soc. Jap.*, 38 (1975) 1220.
96. Jäger, W. and Urban, K., in *Proc. 4th Int. Conf. on High Voltage Electron Microscopy*, Jouffrey B. and Favard P. (Eds.), SFME, Paris, (1976) p. 175.
97. Fujita, H., Sakata, T. and Fukuyo, H., *Jap. J. Appl. Phys.*, 21 (1982) L235.
98. Yin, N.Y., Phillipp, F. and Seeger, A., *Phys. Stat. Sol.*, A116 (1989) 91.
99. Seeger, A., Jin, N.Y., Phillipp, F. and Zaiser, M., *Ultramicroscopy*, 39 (1991) 342.
100. Zinkle, S.J., unpublished research.
101. Watanabe, N., Nishiguchi, R. and Shimomura, Y., *J. Nucl. Mater.*, 179-181 (1991) 905.
102. Flynn, C.P. and Averback, R.S., *Phys. Rev.*, B38 (1988) 7118.
103. Caro, A. and Victoria, M., *Phys. Rev.*, A40 (1989) 2287.
104. Prönnecke, S., Caro, A., Victoria, M., Diaz de la Rubia, T., and Guinan, M., *J. Mater. Res.* 6 (1991) 483.
105. Koponen, I., *Phys. Rev.*, B47 (1993) 14011.
106. Morishita, K., Heinisch, H.L., Ishino, S. and Sekimura N., *J. Nucl. Mater.*, 212-215 (1994) 198.
107. Schilling, W. and Sonnenberg, K., *J. Phys.*, F3 (1973) 322.
108. Rauch, R., Peisl, J., Schmalzbauer, A. and Wallner, G., *J. Phys. Condens. Matt.*, 2 (1990) 9009.
109. Singh, B.N., Leffers, T., and Horsewell, A., *Phil. Mag. A*, 53 (1986) 233.
110. Evans, J.H., in: *Proc. Intern. Conf. on Irradiation Behavior of Metallic Materials for fast Reactor Core Components*, Poirier J. and Dupouy J.M. (Eds.), CEA, Gif-Sur-Yvette, France, 1979, p. 225.
111. Brimhall, J.L. and Simonen, E.P., in: *Proc. Int. Conf. on Defects and Defect Clusters in BCC Metals and Their Alloys*, Nuclear Metallurgy Vol. 18, Arsenault R.J. (Ed.), National Bureau of Standards, Gaithersburg, MD, 1973, p. 321.
112. Mazey, D.J., Eyre, B.L., Evans J.H., Erents S.K., McCracken G.M., *J. Nucl. Mater.*, 64 (1977) 145.
113. Johnson, P.B. and Mazey, D.J., *J. Nucl. Mater.*, 218 (1995) 273.
114. Fleischer, E.L. and Norton, M.G., *Heterogeneous Chemistry Reviews*, 3 (1996) 171.
115. Moteff, J., Sikka, V.K., Jang, H., in: *Consultant Symp. on the physics of irradiation produced voids*, AERE-R7934, R.S. Nelson (Ed.), A.E.R.E. Harwell, 1975, p. 181.
116. Loomis, B.A., Gerber, S.B., Taylor, A., *J. Nucl. Mater.*, 68 (1977) 19.
117. Chen, L.J. and Ardell, A.J., *J. Nucl. Mater.*, 75 (1978) 177.
118. Mazey, D.J., Francis S., Hudson, J.A., *J. Nucl. Mater.*, 47 (1973) 137.
119. Risbet, A. and Levy, V., *J. Nucl. Mater.*, 50 (1974) 116.
120. Horsewell, A. and Singh, B.N., *Radiat. Eff.*, 102 (1987) 1.
121. Farrell, K. and Packan, N.H., *J. Nucl. Mater.*, 85-86 (1979) 683.
122. Zinkle, S.J. and Singh, B.N., *Journal of Nuclear Materials*, 283&287 (2000) 306.
123. Santhanam, A.T., Taylor, A. and Harkness S.D., in: *Proc. Int. Conf. on Defects and Defect Clusters in BCC Metals and Their Alloys*, Nuclear Metallurgy Vol. 18, Arsenault R.J.(Ed.), National Bureau of Standards, Gaithersburg, MD, 1973, p. 302.
124. Nakajima, H., Yoshida, S., Kohno, Y., Matsui, H., *J. Nucl. Mater.*, 191-194 (1992) 952.
125. Johnson, P.B. and Mazey, D.J., *J. Nucl. Mater.*, 93-94 (1980) 721.
126. Johnson, P.B., Thompson, R.W., Mazey, D.J., *Nature*, 347 (1990) 265.
127. Jäger, W. and Roth, J., *J. Nucl. Mater.*, 93-94 (1980) 756.
128. Bullough, R., Eyre, B.L. and Krishan, K., *Proc. Roy. Soc. London*, A346 (1975) 81.
129. Woo, C.H. and Singh, B.N., *Philos. Mag.*, A65 (1992) 889.
130. Singh, B.N. and Foreman, A.J., *Phil. Mag.*, A66 (1992) 975.
131. Golubov, S.I., Singh, B.N. and Trinkaus, H., *J. Nucl. Mater.*, 276 (2000) 78.
132. Ghoniem, N.M., and Gurol, H., *Rad. Eff.*, 55 (1981) 209.
133. Walgraef, D., in *Reactive Phase Formation at Interfaces and Diffusion Processes*, Y. Limoge and J.L. Bocquet (Eds.), Materials Science Forum, 155-156, Trans Tech, Switzerland, pp. 401-408, (1994).
134. Zinkle, S.J., *Fusion Reactor Materials Semiann. Prog. Report for period ending Sept. 30, 1987*, DOE/ER-0313/3, p. 86.
135. Evans, J.H., Bullough, R. and Stoneham, A.M., in: *Radiation induced voids in metals*, CONF-710601, J.W. Corbett and L.C. Iannello (Eds.), National Technical Information Service, Springfield, VA, 1972, p. 522.